photonics

MDPI

Review

Whispering-Gallery-Mode Microcavity Lasers from Visible to Mid-Infrared: Applications

Angzhen Li [1], Yindong Zhang [2,*] and Xiaosong Lu [3,4,*]

[1] Tianjin Key Laboratory of Quantum Optics and Intelligent Photonics, School of Science, Tianjin University of Technology, Tianjin 300384, China; azli@email.tjut.edu.cn
[2] Fujian Provincial Key Laboratory for Soft Functional Materials Research, Department of Physics, College of Physical Science and Technology, Xiamen University, Xiamen 361005, China
[3] Jiangsu Key Laboratory of Advanced Laser Materials and Devices, School of Physics and Electronic Engineering, Jiangsu Normal University, Xuzhou 221116, China
[4] School of Electrical and Electronic Engineering, Nanyang Technological University, Singapore 639798, Singapore
* Correspondence: zhangyindong@stu.xmu.edu.cn (Y.Z.); xingwadyx@jsnu.edu.cn (X.L.)

Abstract

Whispering-gallery-mode (WGM) microcavities, with their ultra-high quality factors and deeply confined mode volumes, provide strong light–matter interaction and underpin a broad range of emerging photonic technologies. Their capabilities now span high-sensitivity sensing, ultra-low-noise microwave and frequency-comb generation, integrated quantum light sources, narrow-linewidth microlasers, and efficient nonlinear frequency conversion. As WGM devices advance toward greater practicality and integration, this paper reviews the research progress of WGM microcavity lasers across the visible to mid-infrared spectrum, which represents a key focus area, and discusses the challenges hindering their broader application.

Keywords: whispering gallery mode; microcavity; laser; visible light; near-infrared light; mid-infrared light

1. Introduction

1.1. Characteristics of Whispering-Gallery-Mode (WGM) Optical Microcavities

WGM microcavities constitute a broad class of resonant structures that confine light via continuous total internal reflection along their curved boundaries, featuring conventional geometries such as microspheres [1], microdisks [2], microrings [3], microtoroids [4], microbottles [5], and microbubbles [6]. One of their characteristics is the ultra-high quality factor (Q-factor), which serves to significantly extend the photon lifetime within the cavity [7,8]. Additionally, WGM microcavities typically exhibit extremely small mode volumes, approaching the diffraction limit [9]. These features enable strong light-–matter interaction. WGM microcavities offer low loss and high integration potential, providing a solid foundation for high-performance photonic devices [10–12].

Since the first report of WGM optical microcavities in 1961 [13], WGM microcavities have remained a major research focus [14–16]. Early studies, primarily involving microspheres and microrings fabricated from various optical materials, greatly advanced our understanding of WGM lasing characteristics [17,18]. In recent years, breakthroughs in micro/nanofabrication technologies such as photolithography and femtosecond laser processing have enabled WGM resonators to shrink in size while maintaining high optical

Check for updates

Received: 4 December 2025
Revised: 29 January 2026
Accepted: 9 February 2026
Published: 10 February 2026

Copyright: © 2026 by the authors. Licensee MDPI, Basel, Switzerland. This article is an open access article distributed under the terms and conditions of the Creative Commons Attribution (CC BY) license.

quality and expanding their practical relevance. Meanwhile, the demonstrated integration of microcavities with optoelectronic components has accelerated progress toward compact and scalable photonic systems [19–22]. In parallel, continued advances in cavity design and material engineering have broadened the accessible wavelength range and functional capabilities of WGM lasers, supporting applications in sensing, nonlinear optics, and related photonic technologies [23–26]. Accordingly, this review summarizes recent advances in WGM microcavity lasers across wavelength-dependent application scenarios from the visible to the mid-infrared.

1.2. Introduction to WGM Microcavity Lasers

Lasers have been widely used in communications [27], industrial processing [28], and healthcare [29]. WGM lasers exhibit ultra-low threshold, narrow linewidth, and compact size, making them ideal light sources for micro/nanophotonic devices [30–32]. Moreover, when the cavity size approaches the lasing wavelength, a variety of novel physical phenomena emerge, which have attracted considerable interest [33,34].

Recent years have seen rapid progress in WGM microcavity lasers across a broad spectral span from the visible to the mid-infrared. This spectral coverage is closely tied to wavelength-dependent applications, as different wavelength bands are associated with distinct performance requirements and use cases. In this review, we therefore consider WGM lasers across the visible to mid-IR range and organize recent advances around representative application scenarios, thereby providing a coherent perspective that bridges fundamental photonics and practical technologies.

Compared with existing reviews that primarily focus on WGM resonators in general, specific cavity geometries, material platforms, or a single spectral window, this review provides an application-driven survey of WGM microcavity lasers from the visible to the mid-infrared. We emphasize wavelength-dependent lasing functionalities and organize the discussion around representative use cases (biophotonics, display and illumination, environmental sensing, optical communications, mid-IR lasing, and nonlinear photonics). Importantly, we relate these demonstrations to deployment-oriented requirements—such as standardized performance benchmarking, scalable fabrication and yield, robust coupling/packaging, stability and noise control, and heterogeneous integration—thereby outlining key gaps and future directions for translating WGM lasers into practical photonic technologies.

2. Basic Principles of WGM Microcavity Lasers

2.1. Wave Optics Theory of WGM Microcavities

Within the framework of electromagnetic theory, WGM microcavities such as microspheres and microbottle have been described by mathematical models [35–37]. For other cavity geometries, numerical methods such as finite element analysis are typically employed. In 1908, Mie first observed spherical microcavitys while studying light scattering by small particles and derived an exact solution based on Maxwell's equations [38,39]. This has become the basis for studying most WGM models. Taking into account the boundary conditions, the electromagnetic field distribution inside the cavity can be written as

$$\Psi = AZ_l(krn_{\text{eff}})P_l^m(\cos\theta)\mathrm{e}^{\pm im\varphi}, \tag{1}$$

where A is a constant and n_{eff} is the effective refractive index, k is the wave number, l is the number of wave nodes along the equatorial circumference, known as the angular mode number, approximated by

$$l = \frac{2\pi r n_{\text{eff}}}{\lambda}. \tag{2}$$

m is the number of nodes along the meridional direction, called the azimuthal mode number, with a range of $-l \leq m \leq l$. $P_l^m(\cos\theta)$ is the associated Legendre function, and $Z_l(krn_{\text{eff}})$ represents the spherical Bessel or Hankel function. After applying boundary conditions, the radial function $Z_l(krn_{\text{eff}})$ can be expressed in a piecewise form:

$$Z_l = \begin{cases} J_l(krn_{\text{eff}}), & r < r_0 \\ J_l(krn_{\text{eff}})\exp[-\alpha(r-r_0)], & r \geq r_0 \end{cases}. \tag{3}$$

$Z_l(krn_{\text{eff}})$ oscillates radially, displaying n successive amplitude maxima. J_l denotes the Bessel function of the first kind of order l. The radial mode number n counts the number of field maxima along the radial direction inside the cavity and thus labels the discrete sequence of radial standing-wave solutions. For a fixed azimuthal and polar order, n = 1 corresponds to the fundamental radial mode whose field peaks closest to the rim, whereas larger n values describe higher-order radial modes that extend further inward and possess increased radial curvature.

Equations (1)–(3) shows that there are n intensity maxima along the radial direction inside the cavity, corresponding to the radial mode number. The field outside the cavity decays exponentially, forming an evanescent surface wave. Thus, a WGM is uniquely determined by the three quantum numbers (l, n, m) and the polarization state.

For TE and TM polarizations, Lam et al. provided asymptotic analytical expressions for the resonant wavelength [40,41]

$$\frac{1}{\lambda} = \frac{1}{2\pi r n_1}\left[\begin{array}{l} l+\frac{1}{2}+2^{-\frac{1}{3}}\alpha(n)\left(l+\frac{1}{2}\right)^{\frac{1}{3}} - \frac{L}{\left(\left(\frac{n_1}{n_2}\right)^2-1\right)^{\frac{1}{2}}} + \\ \\ \frac{3}{10}2^{\frac{2}{3}}\alpha^2(n)\left(l+\frac{1}{2}\right)^{-\frac{1}{3}} - 2^{-\frac{1}{3}}\left(\left(\frac{n_1}{n_2}\right)^2-\frac{2}{3}L^2\right)\frac{\alpha(n)\left(l+\frac{1}{2}\right)^{-\frac{2}{3}}}{\left(\left(\frac{n_1}{n_2}\right)^2-1\right)^{\frac{3}{2}}} \end{array}\right], \tag{4}$$

where r is the sphere radius, λ is the vacuum wavelength, n_1 and n_2 are the refractive indices of the cavity and the surrounding medium, respectively, α_n is the zero of the Airy function, and L is a polarization-dependent coefficient:

$$L = \frac{n_1}{n_2}, \quad \text{(TE mode)}, \tag{5}$$

$$L = \frac{n_2}{n_1}, \quad \text{(TM mode)}. \tag{6}$$

In summary, the electromagnetic field of a microsphere WGM is fully described by four parameters: l, n, m, and polarization. The fundamental mode corresponds to $n = 1$ and $l = m$.

2.2. Key Parameters of WGM Microcavity Lasers

2.2.1. Q-Factor

The Q-factor is a core parameter that reflects the energy storage capability of a WGM microcavity. It encompasses losses due to cavity wall scattering, material absorption, and radiation leakage. A high Q-factor implies longer photon lifetime and lower energy loss, which significantly reduces the lasing threshold and enhances spectral purity and frequency stability. In experiments, the Q-factor is often calculated using

$$Q = \frac{\lambda_0}{\Delta\lambda}, \tag{7}$$

where λ_0 is the resonant wavelength and $\Delta\lambda$ is the full width at half maximum (FWHM) of the microcavity peak.

2.2.2. Lasing Threshold

The lasing threshold is a key indicator of laser performance, defined as the minimum pump energy or power required to achieve stable laser output in a WGM microcavity. Theoretically, the threshold can be derived through numerical simulations considering the microcavity structure and gain medium properties.

Experimentally, it is determined by identifying the critical pump power at which the transition from spontaneous to stimulated emission occurs. Below the threshold, photon loss exceeds stimulated emission. Consequently, the output is dominated by spontaneous emission, which exhibits a broad spectrum and no sharp peaks. At the threshold, stimulated emission surpasses the total photon loss. This imbalance initiates photon amplification, narrows the spectral linewidth, and gives birth to sharp WGM lasing peaks. The emitted light simultaneously acquires improved directionality and well-defined polarization.

2.2.3. Output Wavelength

The output wavelength is closely related to the mode characteristics of the WGM microcavity. Theoretical prediction of the lasing wavelength is based on the theory discussed in Section 2.1. For complex geometries, finite element analysis is often used.

In some application scenarios that only focus on partial patterns, a simplified equation can be used:

$$\lambda = \frac{2\pi n_{\text{eff}} r}{l}, \tag{8}$$

where λ is the output wavelength, n_{eff} is the effective refractive index, r is the cavity radius, and l is the angular mode number.

Tunability of the output wavelength is a key research interest. By adjusting the refractive index of the gain medium, changing the temperature, or applying external stress, fine tuning of the output wavelength can be achieved [42–47], which is valuable in applications such as optical communications and biosensing.

2.2.4. Spectral Linewidth

Spectral linewidth refers to the FWHM of the laser emission peak. It directly reflects the monochromaticity and frequency stability of the laser. A narrower linewidth indicates better spectral purity and stability. High-Q microcavities enable extremely narrow linewidths, which is essential for high-resolution spectroscopy and precision metrology.

In practice, the peak intensity and its center wavelength are first located. After the background noise has been subtracted, the two wavelengths at which the intensity falls to half the maximum are determined. The linewidth is then simply the difference between these two half-intensity points.

2.2.5. Mode Volume

Mode volume describes the spatial confinement of the lasing mode within the WGM microcavity. A smaller mode volume implies higher energy density and stronger light–matter interaction, which can lower the lasing threshold and enhance sensor sensitivity.

For a spherical microcavity, the approximate mode volume of the fundamental WGM is

$$V_{\text{mode}} \approx 4\pi R^2 \delta \tag{9}$$

where $\delta \approx \frac{\lambda}{2\pi\sqrt{n^2-1}}$ is the penetration depth of the evanescent field.

2.2.6. Beam Quality

Beam quality describes the spatial uniformity and far-field propagation characteristics of the laser output. The key metric is the M^2 factor, which quantifies the deviation from an ideal Gaussian beam. For an ideal Gaussian beam, $M^2 = 1$.

The M^2 factor is defined as

$$M^2 = \frac{\theta \cdot w_0}{\lambda / \pi} \tag{10}$$

where θ is the far-field divergence angle, w_0 is the beam waist radius, and λ is the laser wavelength.

Experimentally, M^2 is determined by measuring the beam radius at various positions and fitting the propagation curve:

$$w(z) = w_0 \sqrt{1 + \left(\frac{\lambda z}{\pi w_0^2 M^2} \right)^2} \tag{11}$$

2.3. Excitation Methods of WGM Microcavities

2.3.1. Evanescent Field Coupling

Evanescent field coupling is the most commonly used method for exciting WGM microcavities. This technique facilitates energy exchange between a microcavity and an adjacent waveguide or fiber by exploiting the exponentially decaying electromagnetic field at the cavity surface, enabling efficient and contactless excitation or extraction of WGMs. The coupling strength depends critically on the separation gap and typically requires control at the sub-wavelength scale, often on the order of hundreds of nanometers. Thus, precise alignment is essential for achieving critical coupling. Thanks to its low insertion loss, high directionality, and reversible nature, evanescent-field coupling is widely employed in high-Q WGM-based integrated devices. Importantly, the rapid spatial decay of the evanescent field also minimizes background interference and crosstalk, leading to improved signal-to-noise ratio and enhanced system stability.

Table 1 lists three common evanescent field coupling methods.

Tapered-fiber coupling is one of the most mature and efficient techniques for exciting WGM microcavities via the evanescent field. Its essence is to enhance the evanescent field intensity by drawing a standard single-mode fiber into a conical section through a specialized fabrication process [48,49]. Briefly, the central part of the fiber is first softened by heat and then stretched with a precision pulling stage until a waist diameter of only 0.5–5 μm and a taper length of 2–5 cm are obtained [50,51]. During this process the core diameter is dramatically reduced so that the guided mode—originally confined inside the core—leaks appreciably into the cladding and beyond, producing a markedly stronger evanescent field. A complete coupling process between a tapered fiber and a WGM microcavity can be seen in the work reported by Wang et al., as shown in Figure 1 [52]. In practice, the taper waist is brought into close proximity of the WGM microcavity with the aid of a micro-positioning stage, so that the evanescent field of the taper overlaps spatially with the WGM. When the frequency of the incident light coincides with a WGM microcavity and the phase-matching condition is satisfied, light is transferred efficiently from the tapered fiber to the microcavity, thereby exciting the WGM. Coupling efficiencies as high as ∼99% have been demonstrated [53]. However, the mechanical strength of the tapered fiber is low and its performance is sensitive to environmental vibrations. Consequently, this method is best suited for applications demanding extremely high coupling efficiency, such as high-precision sensing and quantum-optics experiments [8,49].

Planar waveguide coupling is a core approach to realize the on-chip integration of WGM microcavities [54]. Its key lies in integrating the WGM microcavity and the planar

waveguide onto the same substrate. During fabrication, CMOS-compatible processes such as photolithography, etching, or thin-film deposition are first employed to fabricate planar waveguides with specific cross-sections on the substrate [55–57]. Subsequently, WGM microcavities are fabricated adjacent to the waveguides. When the coupling conditions are satisfied, energy can be transferred from the waveguide to the microcavity. Conversely, the energy of WGMs can also be coupled back to the waveguide for output [58]. This approach features high integration density and excellent mechanical stability and can work in synergy with other on-chip components. However, affected by factors such as substrate absorption and fabrication precision, the coupling efficiency is typically in the range of 30% to 80% [59]. It is mainly applicable to scenarios requiring miniaturization and high-density integration [60].

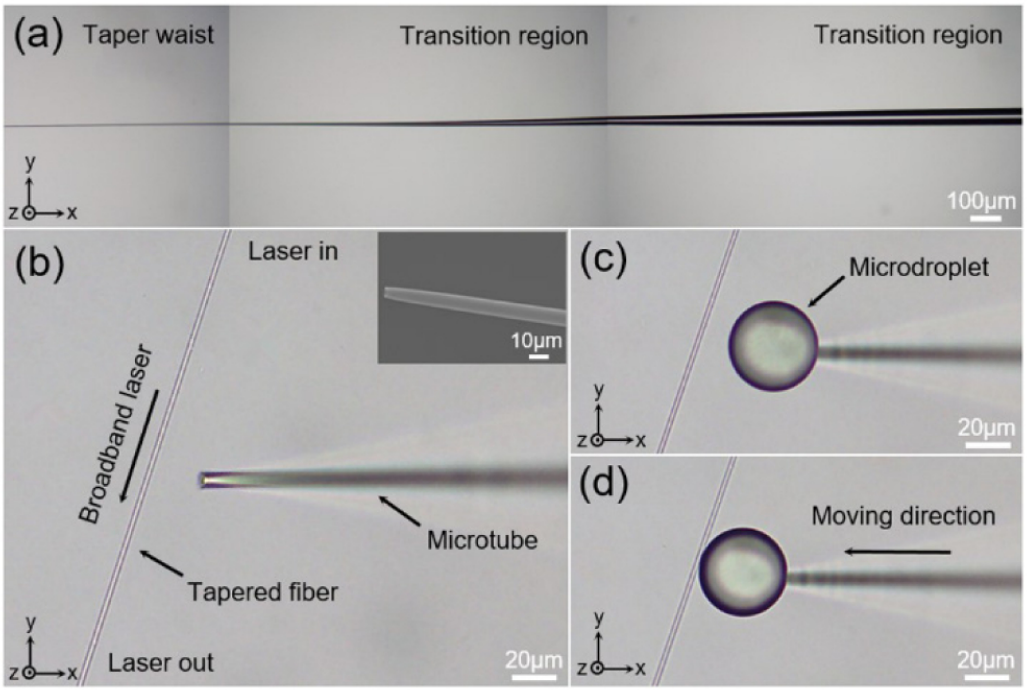

Figure 1. (**a**) Micrographs of different sections of a tapered fiber. (**b**–**d**) Schematic illustration of the coupling process. The figure (**a**–**d**) are reproduced from reference [52].

Prism coupling utilizes the evanescent field generated during total internal reflection of a prism to achieve energy transfer with the WGM microcavity [61]. In this approach, a prism with high refractive index is usually selected, and the bottom surface of the prism is placed parallel to the surface of the WGM microcavity. When light is incident on the bottom surface of the prism at an angle greater than the critical angle between the prism and the surrounding medium, total internal reflection occurs at the bottom surface, generating an evanescent field that propagates along the interface and decays exponentially in the vertical direction. The advantage of prism coupling lies in the ease of adjusting the coupling conditions by changing the incident angle. However, this method has a large volume and low integration density, and its coupling efficiency is typically less than 80% [62–64].

Table 1. Performance comparison of three evanescent field coupling structures.

Coupling Structure	Coupling Efficiency	Integration Level	Mechanical Stability	Application	References
Tapered Fiber	~99%	Low	Low	Laboratory-based research	[8,49,53]
Planar Waveguide	~80%	High	High	On-chip devices	[60]
Prism Coupler	~80%	Low	Medium	High-stability devices	[61,62,64]

2.3.2. Direct Excitation

The direct coupling method focuses the laser directly onto the surface of the microcavity. It utilizes the refraction or scattering to enable part of the photons to enter the microcavity and meet the resonance conditions. This method does not rely on complex evanescent field enhancement structures. In practical, the end face of a single-mode fiber is usually directly attached to the edge of the WGM microcavity [65–67]. Alternatively, during on-chip integration, the output end of the planar waveguide is directly connected to the surface of the microcavity, making the distance between the two approach zero [68,69].

Direct coupling with physical contact often introduces additional scattering losses or absorption losses on the surface of the microcavity, which reduces the Q-factor of the WGM microcavity and further affects the performance of the device, such as sensing sensitivity and filtering accuracy. Therefore, some schemes choose to achieve direct coupling by directly irradiating light onto the surface of the microcavity [70,71]. Figure 2 illustrates an on-chip structure for direct coupling to and excitation of a WGM microcavity [69]. Due to the lack of efficient energy convergence effect of the evanescent field, the coupling efficiency of this method is usually low, generally in the range of 10% to 60% [2,69–72]. In addition, the optical field is prone to generating more stray light during the coupling process, which affects the signal purity.

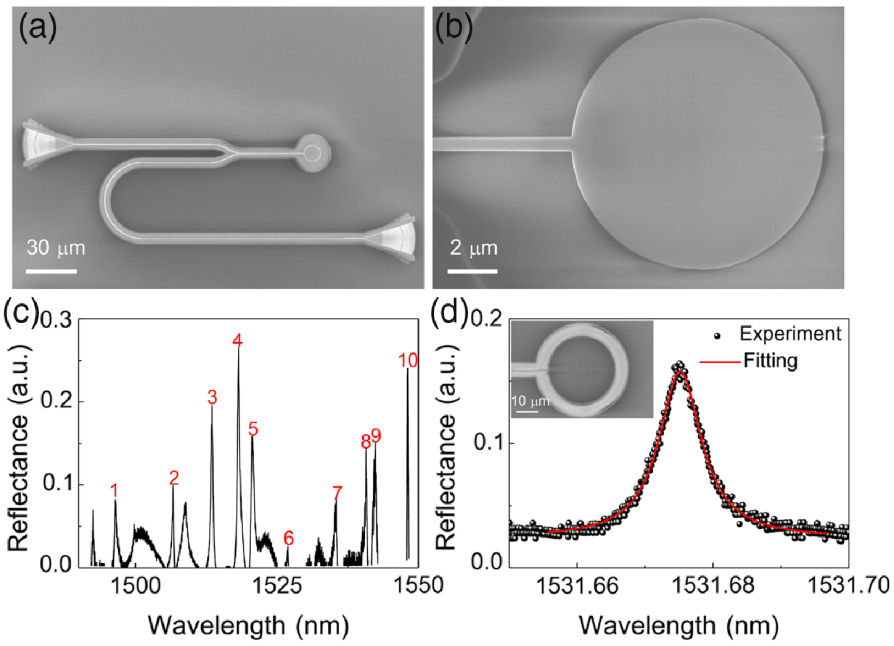

Figure 2. (**a**) Low-magnification top-view scanning electron microscope image showing the overall device architecture, including the input/output waveguides and the microdisk. (**b**) Detailed view of the coupling region. (**c**) Experimentally measured reflection spectrum of the 5 μm radius WCM, exhibiting a series of sharp resonances. Modes labeled 1–10 correspond to quasi-WGM supported by the cavity. (**d**) Magnified view of a single high-quality resonance from a larger WCM with a radius of 15 μm. The figures (**a**–**d**) are reproduced from reference [69].

Despite the obvious drawbacks of direct coupling, it avoids the complex matching process and offers high mechanical stability. Therefore, improving the performance of direct coupling remains a key issue in WGM research. Ward et al. introduced a fiber-tip nano-antenna that excites WGM through cavity-enhanced Rayleigh scattering [72]. By simply positioning a chemically etched single-mode fiber against fused-silica microspheres, they obtained Lorentzian dips, Fano lineshapes, or pure peaks with 13% coupling efficiency while preserving the intrinsic $Q \approx 10^8$ over micrometer scale gaps. Building on this, a WGM

laser packaging method based on the nano-antenna coupler is proposed [73]. The device is compact and fully fiberized and the packaging step leaves the Q-factor almost unchanged.

2.3.3. Electrical Pumping

Electrically pumped WGM lasers represent a paradigm shift toward scalable, chip-scale coherent light sources by enabling direct current injection to achieve population inversion within the resonant cavity. However, the transition toward electrical pumping is essential for practical on-chip photonic integration and scalable device architectures. Electrically pumped WGM lasers integrate semiconductor gain media, such as quantum wells or quantum dots, directly into microdisk, microring, or microsphere resonators, enabling carrier injection through fabricated p-n junctions or lateral contacts [74]. Significant progress has been made in mitigating challenges associated with electrical losses [75], current crowding [76], and thermal management [77], which otherwise degrade the cavity Q-factor and hinder lasing thresholds. Recent demonstrations of room-temperature, continuous-wave electrically pumped WGM lasers in III-V semiconductor platforms underscore their viability for applications in low-power coherent light sources, integrated photonic circuits, and chip-scale sensing [78]. Nevertheless, achieving efficient carrier confinement within the evanescent WGM overlap region while maintaining minimal optical absorption from doped layers remains an active area of research.

3. Applications of WGM Lasers

3.1. Biomolecular Labeling

The principle of biomolecular labeling using WGM lasers relies on their high sensitivity to changes in the local refractive index surrounding the cavity. The narrow linewidth and high brightness of these visible-band lasers enable the transduction of minute biochemical interactions, such as molecular binding, cellular structural changes, or enzymatic activity, into measurable spectral shifts, allowing for high-resolution, often label-free detection and imaging at the single-molecule or single-cell level, including biological specimens such as cells and bacteria [79].

This principle underlies a range of biodetection applications, where WGM lasers are increasingly integrated with hardware and information-processing algorithms [80–82]. For instance, Mai et al. demonstrated biocompatible RhB-doped polymeric microsphere lasers that operate stably in water and undiluted human serum [83], while Zhihe Guo et al. realized label-free sensing in biological buffers using hyperboloid-drum microdisk lasers [84]. Moving beyond external sensing, Schubert et al. embedded microdisk lasers inside cardiomyocytes to convert intracellular refractive-index variations into spectral signals, enabling label-free, all-optical recording of single-cell contractility and sarcomere dynamics [85].

Further advances in device design and integration have expanded these capabilities. Titze et al. developed red-emitting GaInP/AlGaInP quantum-well microdisk lasers with ultra-low thresholds, suitable for deep-tissue and intracellular operation [86]. Figure 3 provides an overview of the laser performance and biocompatibility of these microdisk lasers, along with their intracellular behavior. Subsequently, the same group established a modular protocol for internalizing micro-lasers into cells and tissues, combined with a high-speed hyperspectral imaging system for large-volume, refractive-index mapping and dynamic contraction analysis [87]. In a different approach targeting molecular detection, Wang et al. functionalized a liquid-crystal WGM microcavity to monitor enzymatic reactions in real time via spectral shifts, achieving sensitive detection in serum samples [88]. Together, these works highlight how the fundamental refractive-index sensitivity of WGM lasers is harnessed for diverse, high-precision biomolecular labeling and sensing applications.

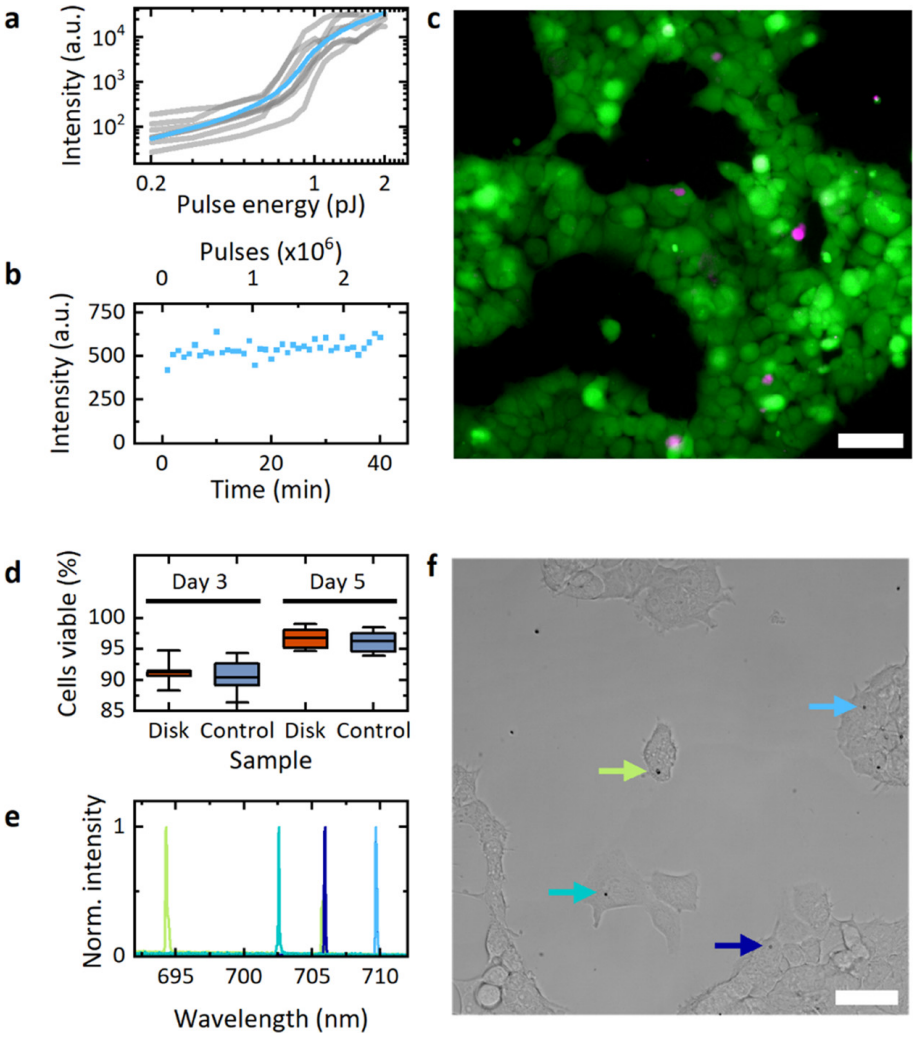

Figure 3. (**a**) Threshold curves of laser emission. (**b**) Stability of laser emission under continuous pumping in an aqueous environment. (**c**) Epifluorescence microscopy image of HEK293 cells incubated with microdisk lasers for 3 days, stained with cell tracker dye (green, live cells) and propidium iodide (magenta, dead cells); scale bar, 40 µm. (**d**) Statistical analysis of cell viability showing no decrease in cells incubated with microlasers for 3 and 5 days compared to control cultures without microlasers; center line represents the mean, box denotes 25–75 percentile, and whiskers represent 1.5 times the standard deviation. (**e**) Normalized lasing spectra of intracellular lasers after 3 days of incubation. (**f**) Brightfield microscope image of HEK293 cells incubated with microdisk lasers; arrows indicate intracellular microlasers with color coding corresponding to spectra in (**e**); scale bar, 50 µm. The figures (**a**–**f**) are reproduced from reference [86].

3.2. Display and Illumination

Visible band lasers are readily detected by most photodetectors and can be directly perceived by the human eye. Consequently, their most prominent characteristic is that they are "visible and accurately measurable". Owing to these features, WGM lasers in the visible band hold exceptional promise for applications in laser-based display technologies.

WGM microcavity lasers can be scaled down to micrometer dimensions and exhibit narrow linewidths (<1 nm) together with high color purity [89,90], making them suitable as pixel elements in micro-display panels. Du et al. constructed heterogeneously coupled microcavitys by contacting dye-doped polymer microspheres of different emission colors and observed tunable RGB single-mode lasing across the full visible range under UV excitation [91]. In the coupled geometry each sphere acted simultaneously as a WGM cavity and as a modulator for its neighbors, suppressing all but one longitudinal mode

regardless of the organic gain medium employed. Jiang et al. reported a continuous wave white microlaser operating at room temperature under 975 nm pump excitation [92]. They co-doped Tm^{3+}, Er^{3+} and Yb^{3+} ions into a single microcavity whose Q-factor approaches 10^8. Under upconversion pumping, the device simultaneously emitted RGB light with microwatt-level thresholds.

Ge et al. fabricated a full-color WGM laser by spatially segregating RGB emitting conjugated polymers inside concentric glass micro-capillaries using a nanosecond pump laser at a wavelength of 343 nm [93]. Under nanosecond optical pumping, the nested cavities simultaneously supported WGMs at three distinct wavelengths, produced linewidths of 0.025 nm, and reached sub-J· cm^{-2} thresholds. Chen et al. employed a surfactant-free self-assembly route to organize RGB colloidal quantum dots into separate WGM microcavities that exhibited mutually matched lasing thresholds [94]. In the experiment, a femtosecond laser with a wavelength of 400 nm was used as the pump. When the RGB cavities were densely integrated on a common substrate, optical cross-absorption was suppressed and the emitters operated almost independently, collectively spanning a color space corresponding to 105% of the BT.2020 gamut. The same microlaser triad was subsequently incorporated as a backlight unit to drive a liquid-crystal display, producing the first full-color prototype powered directly by colloidal quantum dots lasers. Figure 4 shows multicolor laser sources and colloidal quantum dot (CQD) laser backlight displays. In addition, organic semiconductors/polymers offer broad wavelength coverage and low-cost processing for visible WGM lasing, yet operational stability and photobleaching mitigation are critical for practical use.

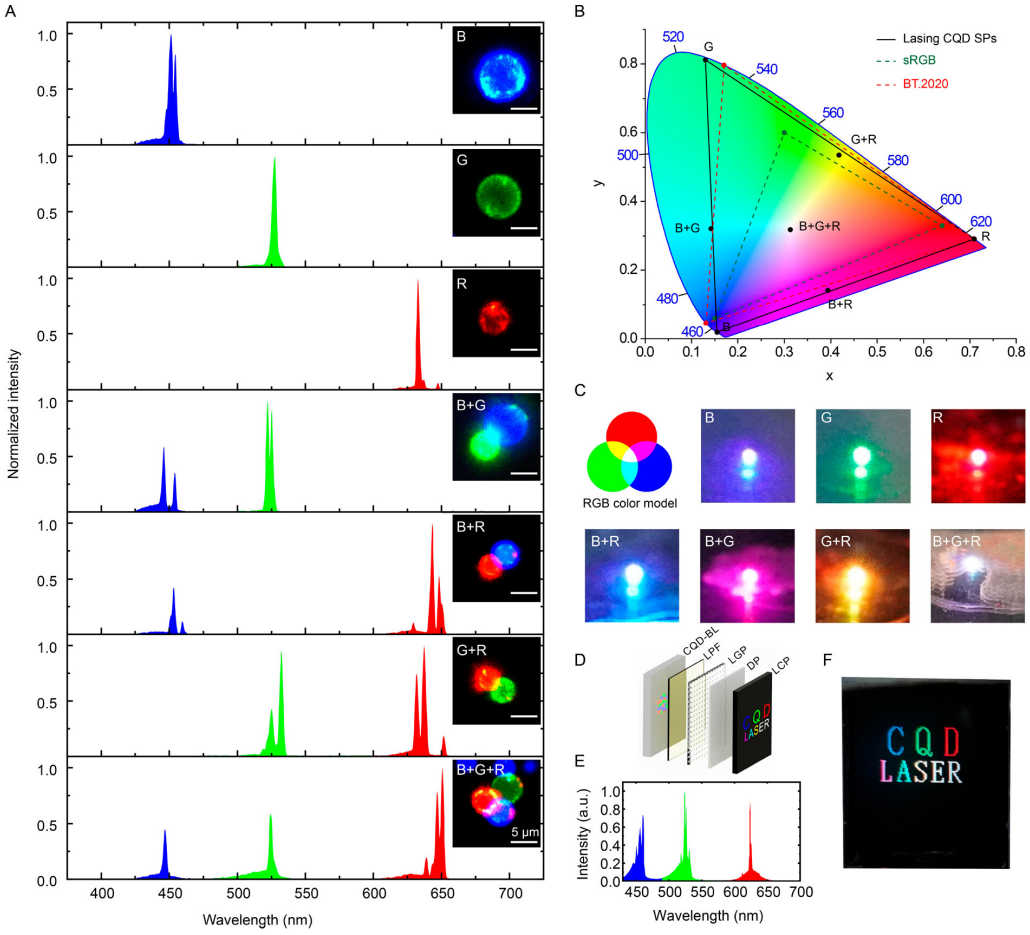

Figure 4. (**A**) Lasing spectra and corresponding optical micrographs of three primary RGB CQD SPs, and their integration under simultaneous excitation above the lasing threshold. (**B**) Chromaticity diagram of the lasing CQD SPs, with sRGB and BT.2020 standards plotted for comparison. (**C**) RGB

color model and far-field photographs of emission light from integrated CQD lasers; additive color lights, including yellow, pink, cyan, and white, can be observed by selectively exciting two or three RGB CQD lasers, consistent with the RGB color model. (**D**) Schematic diagram of the LCD structure using integrated RGB CQD lasers as backlight (CQD-BL: CQD laser backlight; LPF: long-pass filter; LGP: light guide plate; DP: diffuser plate; LCP: liquid-crystal panel). (**E**) Emission spectrum of the integrated CQD laser backlight. (**F**) 1.44 inch full-color LCD utilizing the as-prepared laser backlight. The figures (**A**–**F**) are reproduced from reference [94].

3.3. Environmental Monitoring

The near-infrared band is generally defined as the 0.7–2.5 μm spectral range [95]. This band contains characteristic absorption peaks of various gases, such as CO_2, CH_4, and H_2S [96,97]. The mid-infrared band is typically defined as the 2.5–25 μm spectral range [95]. Within this range, the 3–5 μm window coincides with the fundamental ro-vibrational absorption bands of many molecules. As a result, these spectral windows are of paramount importance for molecular spectroscopic detection and related research fields.

In environmental gas detection based on WGM lasers, an active WGM cavity can be used to self-generate laser emission, whose spectral changes are monitored to infer gas composition. Behsan et al. analytically investigated the gas sensing performance of WGM spherical microlasers that operate on intracavity absorption [98]. They established a compact analytical model to estimate the sensor response. Wu et al. coupled a 1653.72 nm distributed-feedback laser into a high-Q silica microsphere via a tapered fiber [99]. A secondary heating beam, introduced via the supporting fiber, enables thermooptic tuning of the resonance to precisely match the laser wavelength at 1653.72 nm. The enhanced resonant absorption enables the microsphere to function as a compact, fiber-compatible gas sensor with demonstrably improved sensitivity.

An alternative strategy is to couple an external laser to the WGM cavity, thereby exploiting its mode-selection properties for sensing. Han Wang et al. demonstrated a methane sensor based on a high-Q WGM microsphere [100]. It is all-optically tuned so that one resonant mode coincides with the CH_4 absorption line at 1653.72 nm. Figure 5 shows the method of coating microspheres with a metal layer. A simple device is sufficient to perform the coating. Light is launched through the stem of the sphere and partially absorbed by a metallic coating on the crown. The absorbed energy induces localized heating, which in turn increases the refractive index and red-shifts the cavity resonance. Consequently, the photon lifetime inside the cavity lengthens, extending the effective interaction path and enabling sensitive absorption-based detection of methane.

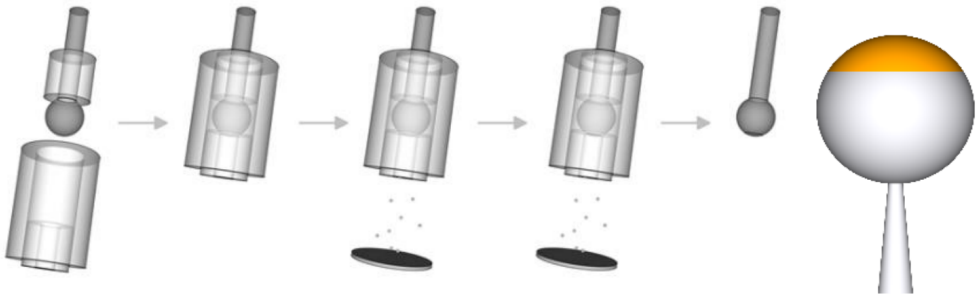

Figure 5. The microsphere is first threaded onto a thin glass tube with an inner diameter of 126 μm and secured. a larger glass tube is then slipped over both the sphere and this supporting tube. A second 126 μm capillary, cut as short as possible, is inserted at the opposite side so that the microsphere is gently clamped between the two miniature tubes while the crown region remains freely exposed inside the larger tube. With the assembly held in this configuration, a metal or high photo-thermal-conversion dielectric film is finally deposited onto the exposed spherical cap by thermal evaporation. The figure is reproduced from reference [100].

WGM microcavity devices are also used to detect other environmental parameters. A thermal infrared detector was realized using a WGM microspherical-shell cavity by V.Sumaria [101]. The device exhibits a temperature-induced resonance shift of 1.17 GHz · K^{-1}. It delivers an experimental responsivity of 7.88 kHz · nW^{-1} and a noise-equivalent power of 19 nW · $Hz^{-1/2}$, corresponding to a detectable displacement of 2 pm. These results demonstrate its capability for sensitive detection across the 1–20 μm spectral range. D'Ambrosio et al. demonstrated a room-temperature photodetector that spans the mid-infrared to terahertz range [102]. The sensor exploits a silica microsphere cavity. A visible free-space laser, frequency-locked to the centre of a WGM, continuously tracks absorption-induced changes in the microcavity's size and refractive index. In this way, the device directly detects quantum-cascade laser beams at 4.3 μm and 111 μm. It enables absorption spectroscopy of the $^{12}CO_2$ fundamental ro-vibrational band as well as weak $^{13}CH_3OH$ rotational transitions. These results illustrate the platform's potential for broadband, high-sensitivity sensing across the mid-infrared and terahertz windows.

3.4. Optical Communications

The near-infrared windows at 1310 nm and 1565 nm constitute the spectral backbone of fiber-optic communications [103]. Owing to their inherently narrow linewidths, long fluorescence lifetimes, and weak environmental sensitivity, rare-earth (RE) ions have become indispensable gain media for lasers and amplifiers operating in the telecommunications window [104,105]. Specifically, the $^4I_{13/2} \rightarrow {}^4I_{15/2}$ transition of Er^{3+} spans the C-band (1530–1565 nm) [106], whereas the $^3F_4 \rightarrow {}^3H_6$ transition of Tm^{3+} covers the S-band (1460–1530 nm) [107]. By doping the WGM host with RE ions or monolithically integrating a semiconductor gain segment, compact near-infrared optical amplifiers and lasers can be realized [108,109]. These devices serve as light sources or in-line repeaters, substantially reducing form factor and power consumption in optical networks. Table 2 lists the emission peaks of RE ions corresponding to the communication band. Yang et al. demonstrated that a microbubble WGM cavity can be converted into an active device by depositing an Er^{3+}-doped sol–gel layer onto a tapered microcapillary before blowing the microbubble [110]. During fabrication, the RE ions diffuse into the 1.3 μm thick silica wall, and pumping at 980 nm produces stable laser emission at 1535 nm from the WGM. Aerostatic pressurization of the internal cavity shifts the modal frequencies, yielding a continuous wavelength tuning range of 240 pm under 2 bar without measurable degradation of the quality factor. Li et al. reported a Tm^{3+}-Ho^{3+}-codoped tellurite glass microsphere that, when pumped at 802 nm through a tapered microfiber, generates both multimode and single-mode laser emission centered at 1.47 μm [111]. Several types of Tm^{3+} lasers near 1675 nm have been reported [112]. However, WGM lasers in this regime remain relatively rare.

Beyond RE ions, WGM lasers based on transition-metal and other dopants have also attracted attention. Fang et al. fabricated multicomponent germanate glass microspheres in which bismuth ions are homogeneously retained without metallic precipitation [113]. When one such sphere is evanescently coupled to a fiber taper, 808 nm pumping elicits WGM laser emission at 1305.8 nm with an absorbed-power threshold of 215 μW. Quantum dot materials are also used as gain media for WGM lasers. Wan et al. demonstrated electrically pumped micro-lasers employing quantum dot active regions heteroepitaxially grown directly on industry-standard (001) silicon substrates [114]. These devices achieved continuous-wave lasing at ∼1.3 μW with operation up to ∼100 °C. A ∼5 μW radius microlaser achieved a submilliamp threshold of ∼0.6 μA, with both threshold current and device footprint reduced by orders of magnitude compared to prior epitaxial lasers on silicon.

Table 2. RE ions emission peaks in the communication band (1350–1675 nm).

Ion	Transition	Center Wavelength (nm)	Remarks	References
Nd^{3+}	$^4F_{3/2} \rightarrow {}^4I_{13/2}$	~1350	Overlaps O-band edge; suffers from ESA	[105]
Tm^{3+}	$^3H_4 \rightarrow {}^3F_4$	1460–1490	1470 nm window for S-band extension	[111]
Er^{3+}	$^4I_{13/2} \rightarrow {}^4I_{15/2}$	1530–1565	C-band and L-band of silica EDFA	[108–110]
Tm^{3+}	$^3F_4 \rightarrow {}^3H_6$	~1675	Beyond water peak; needs low-phonon glass	[112] (without WGM)

Taken together, WGM lasers in the communication band have currently been well realized, providing favorable conditions for their application in various optical communication devices. However, the integration of WGM lasers with other communication components and the interference resistance of WGM devices are key issues that need to be addressed in the future. In addition to conventional RE ions, halide perovskites have emerged as promising visible and NIR gain media for WGM microcavity lasing due to their high optical gain and bandgap tunability, although stability remains a key challenge [115,116]. Furthermore, two-dimensional materials are increasingly explored in hybrid WGM platforms, leveraging strong excitonic responses and ease of integration, while thermal and uniformity issues remain to be addressed [117].

3.5. A Platform for Mid-Infrared Laser-Material Research

Research on mid-infrared laser materials is confronted with multiple challenges. The material systems for mid-infrared WGM lasers primarily include fluoride crystals, chalcogenide glasses, RE-doped oxides, as well as emerging two-dimensional materials and semiconductor heterostructures. In terms of fabrication techniques, researchers have successfully produced high-quality microcavities with sub-nanometer surface roughness using methods such as femtosecond laser direct writing [118], focused ion beam etching, thermal reflow shaping [119] and chemical vapor deposition [120]. Although some mid-infrared glass materials have been used to fabricate WGM microcavity lasers, the lasing wavelengths of certain devices still operate in the visible or near-infrared range [121], highlighting the significant technical challenges that remain in realizing WGM lasers in the mid-infrared spectral region. In RE-doped systems, multiphonon relaxation rises sharply and the upper-level lifetime drops precipitously as the emission wavelength extends. Moreover, mid-infrared laser materials are often mechanically fragile and chemically unstable, making them difficult to fabricate and reprocess. These issues render the development of mid-infrared materials and devices exceptionally demanding [122–125].

As discussed earlier, WGM microcavities enhance light-matter interaction. Moreover, some WGM resonators can be fabricated via simple procedures, which significantly facilitates the investigation of performance in novel mid-infrared laser materials. Earlier studies focused on integrating mid-infrared materials into WGM microcavities to achieve laser emission. Consequently, the majority of the emission wavelengths fell in the near-infrared range. As a result, the superior properties of fluoride and chalcogenide glasses were not fully exploited [126–129].

In recent years, an increasing number of WGM lasers operating in the mid-infrared region have been reported. In 2014, Deng et al. demonstrated a mid-infrared ZBLAN glass microsphere laser [130]. Using a 980 nm laser to pump an Er^{3+}-doped ZBLAN glass microsphere resonator, they achieved lasing at approximately 2.7 μm with a threshold power below 150 μW. Tatiana et al. introduced a melt-drawing technique that converts commercial ZBLAN fiber into microspheres 250–350 μm in diameter [131]. The spheres support WGM with intrinsic quality factors of $(5.4 \pm 0.4) \times 10^8$ at 1.55 μm, a value limited

only by the bulk material loss. At 2.64 μm the same fabrication route yields Q-factors above 10^8, matching the highest mid-infrared figures reported for any microcavity platform. A. Razova et al. optically pumped HgCdTe microdisks 50 μm in diameter and achieved WGM lasing near 4 μm [132]. Auger-suppressed quantum wells extended the operating temperature to 230 K, just 40 K below the spontaneous-emission quench point of the unpatterned epilayer. Throughout the thermoelectric-cooling range, the emission spectrum showed multimode peaks 0.37 meV wide.

S. Katharina et al. demonstrated a continuous-wave WGM parametric oscillator based on a 3.5 mm $AgGaSe_2$ disk pumped at 1.57 μm [133]. The simplified sketch of experimental setup is shown in Figure 6. The device oscillates at milliwatt thresholds and delivers 10–800 μW of idler power. By selecting the radial pump mode, the output wavelength reaches 8 μm. A 100 nm continuous shift is obtained through temperature tuning. Simulations predict that reducing the disk diameter to ∼2 mm extends the idler beyond 10 μm.

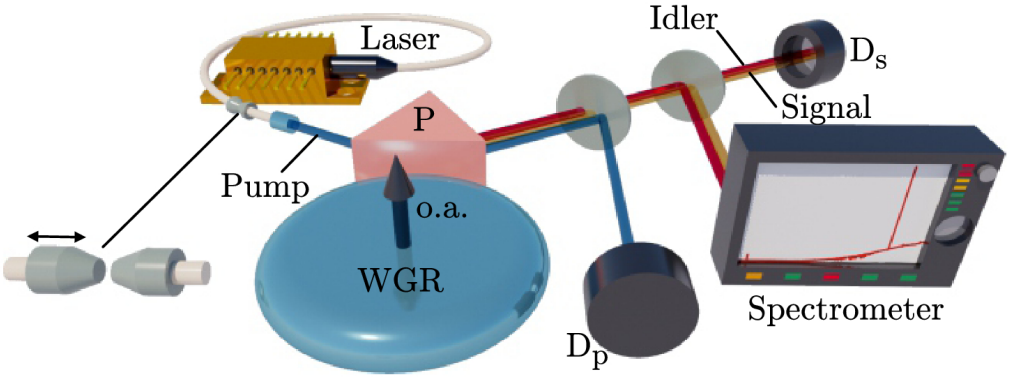

Figure 6. Simplified sketch of experimental setup. Pump light is coupled into an $AgGaSe_2$ WGM cavity via a silicon prism (P). Pump power is adjusted by fiber-end distance. Signal, idler waves, and remaining pump light are detected by a spectrometer, photodetectors D_s and D_p, respectively. The WGM cavity's optical axis (o.a.) aligns with the resonator's symmetry axis. The figure is reproduced from reference [133].

Group IV semiconductor microcavity lasers have emerged as promising platforms for mid-infrared coherent light sources, with recent advances highlighting the critical role of pumping schemes in device performance and integrability [134,135]. While optically pumped configurations often rely on complex, external pump lasers, introducing substantial energy losses, thermal burdens, and system bulk, electrically pumped architectures offer a compelling alternative by enabling direct carrier injection, enhanced electrical-to-optical efficiency, and compatibility with standard planar semiconductor processes for monolithic integration. Notably, Teren et al. demonstrated electrically pumped GeSn (14 at.% Sn) micro-ring lasers on Si, where careful control of cavity undercut and geometry enabled lasing in devices up to 40 μm in radius with a tenfold reduction in threshold current density relative to smaller counterparts, underscoring the strong interplay between thermal management and cavity design [136]. Complementing this, Kryzhanovskaya et al. reported electrically driven InGaAs/GaAs quantum well microdisk lasers monolithically integrated on (001) Si via Ge buffer layers, achieving room-temperature pulsed lasing at threshold current densities as low as 28 kA/cm^2 and narrow linewidths (∼35 pm) in single-mode operation [137]. Beyond conventional planar geometries, Wu et al. engineered three-dimensional tubular micro-resonators by rolling up GeSn/Ge nanomembranes, realizing high-quality-factor WGM cavities with diameters of ∼7.3 μm, where strain-engineered radial profiles, verified by micro-Raman spectroscopy, further enrich the design space for Group IV infrared photonics [138].

3.6. Applications of WGM Microlasers in Nonlinear Optics

Nonlinear optical phenomena such as Raman and Brillouin scattering based on WGM microcavities have been realized across multiple wavelength bands [139–145]. Jiang et al. demonstrated Raman lasing at 1550 nm in a slightly deformed silica micro-cavity [146]. The cavity was pumped through free-space coupling, and the absorbed pump threshold was only 100 μW. This ultralow value reflects WGM quality factors above 10^8. The authors further verified that the threshold scales inversely with the square of the intrinsic quality factor, in agreement with theory.

In stimulated Brillouin scattering, WGM microcavities enable efficient coupling between optical and acoustic phonons through opto-mechanical interaction, giving rise to GHz-frequency phonon lasers and Brillouin-optical oscillators. Tian et al. fabricated a z-cut MgF_2 WGM cavity with a radius of 180 μm and a Q-factor above 10^8 at 1550 nm [147]. By sweeping the pump-cavity detuning, they simultaneously excited stimulated Brillouin and Raman lasers. The Brillouin shift matched the calculated gain bandwidth, while the Raman shift coincided with the A_{1g} symmetric stretching mode of the crystal. Under the same excitation map, four-wave-mixing sidebands emerged, evidencing cascaded nonlinear conversion in the high-Q microcavity.

In the realm of optical parametric oscillation, the strong $\chi^{(2)}$ and $\chi^{(3)}$ nonlinearities accessible in WGM geometries have revolutionized frequency-comb technology [148–150]. Chen et al. reported a III-V integrated nonlinear ring cavity [151]. An angular grating embedded in the resonator imprints a unique orbital angular momentum value on each line of the on-chip generated frequency comb. This process yields 50 distinct orbital angular momentum modes, which collectively form a spatiotemporal "light spring". By tailoring the intermodal phase relationship, the authors further sculpted the emission into optical pulses whose orbital angular momentum evolves over time. Wang et al. demonstrated stimulated Raman comb generation in a WGM microcavity excited by higher-order transverse modes [152]. By tuning the pump detuning, they reversibly switched the comb between multi-mode and single-mode regimes. As the intracavity power was increased to approximately ~200 mW, the spectral bandwidth of the single-mode comb progressively expanded. Ultimately, the stimulated Raman comb merged with the Kerr comb, yielding a seamless octave-spanning optical frequency comb extending from ~1515 nm to ~1700 nm. Song et al. demonstrated an integrated frequency comb on thin-film lithium niobate that overcame the conventional spacing-span tradeoff by sequentially combining dissipative Kerr soliton generation with electro-optic phase modulation [153]. This dual-effect approach produced 2589 comb lines spaced by 29.308 GHz, spanning 75.9 THz (588 nm), while the electro-optic effect provided electronic stabilization and control of the comb spacing. The Figure 7 illustrates the hybrid Kerr-EO frequency comb, including its components, photonic chips, resonator and modulator images, cross-sectional schematics, generation process, and defined variables.

These advances are rooted in the extreme field enhancement offered by WGM cavities, which reduces the threshold for nonlinear processes to microwatt-level pump powers and thereby drastically lowers overall system energy consumption.

To facilitate a more intuitive comparison across representative WGM microcavity laser demonstrations, we summarize key quantitative metrics in Table 3, including the resonator size, Q factor, lasing threshold, and spectral coverage. It should be noted that these metrics are not always directly comparable across reports because they can depend strongly on cavity geometry, coupling conditions, pumping schemes, and the specific definitions adopted by different authors (e.g., threshold reported as coupled pump power versus incident pump power, or as power versus fluence). Therefore, the values in Table 3 are compiled as representative metrics as reported in the original references, and we use

"-" where a given metric is not explicitly provided. Despite these limitations, the table provides a useful quantitative snapshot of typical performance levels and the operating wavelength ranges across different device and application categories.

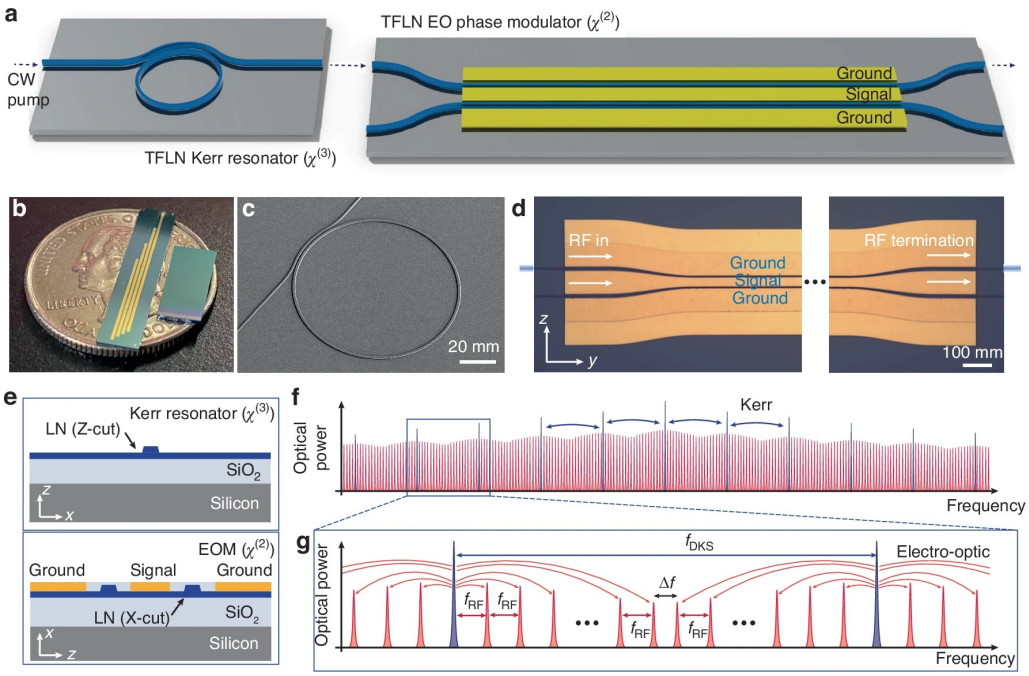

Figure 7. (**a**) Three-dimensional illustration of the hybrid Kerr electro-optic frequency comb composed of a DKS microresonator chip and an electro-optic phase modulator chip. (**b**) Photograph of thin-film lithium niobate photonic chips with an electro-optic phase modulator array (**left**) and Kerr resonators (**right**). (**c**) Scanning electron microscope image of the Kerr resonator. (**d**) Optical microscope image of two parallel electro-optic phase modulators. (**e**) Cross-sectional schematic of the Kerr resonator (**top**) and the electro-optic phase modulator (**bottom**) with crystal axes labeled. (**f**) Schematic of the hybrid Kerr electro-optic frequency comb generation process. (**g**) Schematic of variables defined in this work. The figure is reproduced from reference [153].

Table 3. Quantitative comparison of representative WGM microcavity lasers (as reported in the literatures; SBS—stimulated Brillouin scattering, SRS—stimulated Raman scattering).

Application Category	Cavity Size	Q	Laser Threshold	Spectral Coverage λ (μm)	References
Biomolecular Labeling	82 μm	$\sim 2.4 \times 10^3$	~ 23.2 μJ mm^{-2}	~0.62	[83]
Display and Illumination	53 μm	$(1.8 \pm 0.15) \times 10^8$	8 mW	white light	[92]
Environmental Monitoring	190 μm	4×10^6	–	IR-THz	[102]
Optical Communications	-	10^5	1.5 mW	1.47	[111]
Mid-IR Laser-Material Research	310 μm	$(1.13 \pm 0.22) \times 10^8$	–	2.64	[131]
Nonlinear Optics	180 μm	2×10^8	SBS: ~3.4 mW; SRS: ~8.1 mW	1.55	[147]

Recent years have witnessed rapid progress in emerging materials for visible and NIR WGM lasers. Halide perovskites have attracted strong interest due to their high optical gain, bandgap tunability, and processing compatibility, enabling low-threshold microcavity lasing in representative demonstrations; however, photostability and environmental robustness remain key challenges for practical deployment. Two-dimensional materials (e.g., transition-metal dichalcogenides) offer strong excitonic light-matter interaction and integration flexibility, providing opportunities for hybrid WGM lasers and compact on-chip implementations, while thermal dissipation, material uniformity, and scalable integration are still under active development. Organic semiconductors and polymers provide broad spectral coverage and potentially low-cost fabrication, yet their operational stability and photobleaching/thermal effects require further improvement [154]. Overall, these emerging platforms, together with mature semiconductor and glass/crystal systems, motivate heterogeneous integration as an important trend for achieving stable, scalable, and application-ready WGM lasers.

4. Current Status and Challenges

WGM microcavity lasers have progressed from early proof-of-concept demonstrations to enabling a broad range of photonic functionalities. As summarized in Table 4, representative studies have demonstrated their utility in bio-related labeling and imaging, narrow-linewidth emission for display-oriented light sources, trace-gas sensing enabled by high-Q resonant transduction from the visible to the mid-infrared, low-threshold light generation in telecom-relevant bands for integrated photonics, mid-infrared lasing in selected material platforms, and cavity-enhanced nonlinear optics such as reduced-threshold comb generation and structured-light emission. Together, these advances highlight WGM lasers as a versatile microcavity platform bridging fundamental photonics and emerging applications.

Table 4. Summary and outlook for WGM microcavity lasers.

Application Category	Key Characteristics	Key Gaps/Bottlenecks	Future Directions	Representative Recent Works
Biomolecular Labeling	Ultra-narrow linewidth and high brightness for spectral barcodes and single-cell tracking; RI sensitivity enables label-free optical readout; stability in physiological media supports long-term monitoring.	Biofluid-induced drift (adsorption/fouling); scalable, reproducible barcode libraries; biocompatible encapsulation/clearance; lack of standardized decoding/benchmarking.	Anti-fouling passivation and encapsulation; standard barcode metrics/decoding; scalable fabrication/sorting with uniform linewidth; referencing/drift compensation for long-term use.	[83,85–88]
Display and Illumination	Sub-nm linewidth for high color purity; microcavities as micrometer-scale pixels; full visible RGB with gamut > BT.2020 for microdisplays/backlights.	Visible electrical pumping; heat and lifetime at high brightness; wafer-scale uniform arrays/yield; packaging and beam shaping/speckle control.	Electrically pumped or heterogeneously integrated RGB platforms; thermal-aware cavity/package design; array-level process control and test standards; engineered out-coupling for display-ready emission.	[91–94]
Environmental Monitoring	High-Q resonance shifts for trace-gas sensing (intracavity absorption); thermo-optic/photothermal tuning for molecular fingerprints; extendable to mid-IR/THz; compact/fiber-compatible.	Field robustness (T/vibration/contamination); lab-fragile coupling/packaging; mid-IR low-loss materials/components; calibration and standardized reporting.	Hermetic packaging and thermal/mechanical isolation; integrated couplers and reference/locking channels; low-loss mid-IR platforms; standardized calibration and stability benchmarks.	[100–102]

Table 4. *Cont.*

Application Category	Key Characteristics	Key Gaps/Bottlenecks	Future Directions	Representative Recent Works
Optical Communications	Telecom-band emission; narrow linewidth and low threshold for DWDM/coherent links; compatibility with silicon photonics for on-chip sources.	Packaging-ready coupling; stable single-mode/low noise; wafer-scale reproducibility/yield; integration with tuning, modulators, and electronics.	On-chip/fiber-attachable couplers and robust packaging; mode engineering and thermal tuning/feedback locking; wafer-scale process control; system co-design with PICs/electronics.	[110,111,113,114]
Mid-IR Laser-Material Research	WGM feedback boosts gain efficiency in fragile mid-IR materials; compact testbed for new gain media and mid-IR resonator platforms.	Mid-IR absorption/scattering and thermal load; humidity/contamination sensitivity; limited pumps/couplers; insufficient long-term reliability data.	Lower-loss processing and better heat sinking; mid-IR coupler/packaging solutions; pump co-integration; reliability protocols (aging/thermal cycling/humidity) and standardized reporting.	[130–133]
Nonlinear Optics	Strong confinement lowers nonlinear thresholds to μW level; enables Raman/Brillouin/Kerr/FWM; supports combs and structured light via mode engineering.	Dispersion and mode crossings; thermal instabilities; coherence/phase-noise control; repeatability; integration with pumps and control loops.	Dispersion-engineered cavities and mode management; thermal stabilization and feedback locking; standardized coherence/phase-noise metrics; reproducible fabrication and hybrid integration with pumps/control electronics.	[146,147,152,153]

Looking ahead, translating WGM lasers from laboratory demonstrations to scalable and field-deployable devices requires addressing several cross-cutting gaps. First, many high-Q microcavities still rely on manual or platform-specific fabrication routes, highlighting the need for standardized and scalable processes that deliver tight dimensional control, high yield, and reproducible Q factors across batches. Second, robust coupling and packaging remain limiting factors: while sensitivity to temperature, vibration, and surface adsorption underpins sensing, the same sensitivities complicate stable operation in non-laboratory environments. Future work should therefore prioritize hermetic or application-specific packaging, thermo-mechanical isolation, and active stabilization/locking strategies, together with quantitative long-term drift and reliability benchmarks. Third, visible-to-mid-infrared applications often require heterogeneous material choices such as Si/SiN, $LiNbO_3$, III-V semiconductors, and soft-glass platforms, yet efficient low-loss interfacing across these platforms remains challenging [155–157]. Developing heterogeneous integration and hybrid coupling schemes that preserve optical compatibility, stability, and manufacturability will be central to building multifunctional, multiwavelength WGM systems for complex photonic integrated circuits.

In addition, consistent benchmarking and reporting (e.g., threshold definitions, coupling conditions, linewidth/noise and stability metrics) would greatly improve cross-platform comparability. Finally, system-level integration-including pumping schemes, thermal management, and array-level control-remains a key direction for practical deployment.

5. Summary

Thanks to their ultra-high Q-factors, near-diffraction-limited mode volumes, and facile integrability, WGM microcavities have emerged in recent years as a central platform

for advances in optics, quantum information, and nonlinear photonics. Current WGM-based devices still face challenges, including suboptimal cavity coupling efficiency and stability, stringent fabrication requirements for ultra-high-Q resonators, intrinsic absorption losses in semiconductor materials, and thermal effects and mode competition in nonlinear processes. As a highly controllable, strongly field-enhancing, and energy-efficient optical platform, WGM microcavities are gradually reshaping the design paradigm of micro- and nanoscale photonic devices. From microlasers to optical frequency combs, and from single-molecule detection to quantum optics, the development of WGM microcavities is still rapidly expanding, with their full potential yet to be realized.

Author Contributions: Writing—original draft preparation, A.L.; writing—review and editing, A.L., Y.Z. and X.L.; designed the overall structure of the review, Y.Z. and X.L. All authors have read and agreed to the published version of the manuscript.

Funding: This work was financially supported by the National Natural Science Foundation of China (62305137).

Data Availability Statement: All data are included in the manuscript amd no additional data are required.

Acknowledgments: All figures marked with "CC BY 4.0 License" are used in accordance with the terms of the Creative Commons Attribution 4.0 International License. For other figures, written permission to reproduce has been obtained from the respective copyright holders, and all relevant permissions are retained by the authors.

Conflicts of Interest: The authors declare no conflicts of interest.

References

1. Ward, J.; Benson, O. WGM microresonators: Sensing, lasing and fundamental optics with microspheres. *Laser Photonics Rev.* **2011**, *5*, 553–570. [CrossRef]
2. To, C.H.; Fu, W.Y.; Li, K.H.; Cheung, Y.F.; Choi, H.W. GaN microdisk with direct coupled waveguide for unidirectional whispering-gallery mode emission. *Opt. Lett.* **2020**, *45*, 791–794. [CrossRef] [PubMed]
3. Chen, J.; Nasir, A.; Abazi, A.; Eich, A.; Sánchez-Postigo, A.; Takeda, H.; Mikami, Y.; Tate, N.; Oki, Y.; Yamamoto, Y.; et al. Coexistence of the Radial-Guided Mode and WGM in Azimuthal-Grating-Integrated Microring Lasers. *ACS Photonics* **2024**, *11*, 5110–5117. [CrossRef]
4. Suebka, S.; McLeod, E.; Su, J. Ultra-high-Q free-space coupling to microtoroid resonators. *Light Sci. Appl.* **2024**, *13*, 75. [CrossRef] [PubMed]
5. Sumetsky, M. Lasing microbottles. *Light Sci. Appl.* **2017**, *6*, e17102. [CrossRef]
6. Shen, Y.; Wang, Z.; R, A.V.; Wang, Z.; Jibon, R.H.; Rout, A.; Cai, B.; Wu, Q.; Semenova, Y. Enhanced Force Sensing Utilizing a Glass-Supported WGM Microbubble Resonator. *J. Light. Technol.* **2025**, *43*, 5989–5995. [CrossRef]
7. Fu, B.; Gao, R.; Lin, J.; Yao, N.; Zhang, H.; Wang, M.; Qiao, L.; Fang, W.; Cheng, Y. Modes Trimming and Clustering in a Weakly Perturbed High-Q Whispering Gallery Microresonator. *Laser Photonics Rev.* **2023**, *17*, 2300116. [CrossRef]
8. De Oliveira, R.; Colombano, M.; Malabat, F.; Morassi, M.; Lemaître, A.; Favero, I. Whispering-Gallery Quantum-Well Exciton Polaritons in an Indium Gallium Arsenide Microdisk Cavity. *Phys. Rev. Lett.* **2024**, *132*, 126901. [CrossRef]
9. Jiang, X.; Yang, L. Optothermal dynamics in whispering-gallery microresonators. *Light Sci. Appl.* **2020**, *9*, 24. [CrossRef]
10. Yu, D.; Chen, J.; Zhang, S. Active whispering-gallery microclock in pulsed-operation mode. *Phys. Rev. A* **2023**, *107*, 043712. [CrossRef]
11. Guan, J.; Yang, Z.; Yu, H.; Wang, Z.; Tang, X.; Zhao, Q.; Wang, C.; Zhao, G.; Li, M.; Zhang, J. Magnetostrictive-Assisted Whispering Gallery Mode Sensors. *Photonic Sens.* **2025**, *15*, 250316.
12. Caixeiro, S.; Dörrenhaus, R.; Popczyk, A.; Schubert, M.; Kath-Schorr, S.; Gather, M.C. DNA Sensing with Whispering Gallery Mode Microlasers. *Nano Lett.* **2025**, *25*, 4467–4475. [CrossRef] [PubMed]
13. Garrett, C.G.B.; Kaiser, W.; Bond, W.L. Stimulated Emission into Optical Whispering Modes of Spheres. *Phys. Rev.* **1961**, *124*, 1807–1809. [CrossRef]
14. Liu, B.; Liu, S.; Zhang, Q.; Hong, G.; Liao, C.; Xu, X.; Liu, L.; Qu, J.; Wang, Y. Microbubble-probe WGM resonators enable displacement measurements with high spatial resolution. *Opt. Lett.* **2023**, *48*, 1922–1925. [CrossRef] [PubMed]

15. Guan, B.; Kok, T.W.; Riesen, N.; Lancaster, D.; Suu, K.; Priest, C. Microsphere-Enabled Micropillar Array for Whispering Gallery Mode Virus Detection. *ACS Appl. Mater. Interfaces* **2024**, *16*, 12042–12051. [CrossRef]
16. Yao, J.; Liu, B.; Liu, Z.; Xie, X. Characterization of humidity sensing based on optical microbubble resonators. *Opt. Express* **2025**, *33*, 36632–36645. [CrossRef]
17. Li, H.; Hao, S.; Qiang, L.; Li, J.; Zhang, Y. Observation of whispering gallery modes in microtube-microspheres system. *Appl. Phys. Lett.* **2013**, *102*, 231908. [CrossRef]
18. Liu, S.; Shi, B.; Wang, Y.; Cui, L.; Yang, J.; Sun, W.; Li, H. Whispering gallery modes in a liquid-filled hollow glass microsphere. *Opt. Lett.* **2017**, *42*, 4659–4662. [CrossRef]
19. Tamboli, A.C.; Haberer, E.D.; Sharma, R.; Lee, K.H.; Nakamura, S.; Hu, E.L. Room-temperature continuous-wave lasing in GaN/InGaN microdisks. *Nat. Photonics* **2007**, *1*, 61–64. [CrossRef]
20. Wolf, R.; Jia, Y.; Bonaus, S.; Werner, C.S.; Herr, S.J.; Breunig, I.; Buse, K.; Zappe, H. Quasi-phase-matched nonlinear optical frequency conversion in on-chip whispering galleries. *Optica* **2018**, *5*, 872–875.
21. Dong, J.; Liang, Z.; He, C.; Liu, N.; Chen, Z.; Wang, Q.; Zhang, K.; Xu, C.; Wang, X. Core-Shell Microdisk with InGaN/GaN Quantum Wells for Dual-Band WGM Lasing. *Chip* **2025**, *5*, 100150. [CrossRef]
22. Huang, X.; Horder, J.; Yamamura, K.; Wong, W.W.; Aharonovich, I.; Wang, N.; Jagadish, C.; Tan, H.H. Bottom-up Single Quantum Dots in Microring Resonators for On-Chip Integrated Single Emitters. *Nano Lett.* **2025**, *25*, 6318–6324. [CrossRef] [PubMed]
23. Zhang, M.; Yang, W.; Tian, K.; Yu, J.; Li, A.; Wang, S.; Lewis, E.; Farrell, G.; Yuan, L.; Wang, P. In-fiber whispering-gallery mode microsphere resonator-based integrated device. *Opt. Lett.* **2018**, *43*, 3961–3964. [CrossRef] [PubMed]
24. Liu, X.; Cui, X.L.; Wang, D.N. Integrated in-fiber coupler for a whispering-gallery mode microsphere resonator. *Opt. Lett.* **2020**, *45*, 1467–1470. [CrossRef]
25. Mei, Y.; Wang, D.N.; Wang, Q.; Zhang, Y. Whispering gallery mode microsphere resonator based on cylindrical air cavity coupling. *Opt. Lett.* **2023**, *48*, 1594–1597. [CrossRef]
26. Tian, C.; Becker, P.; Bohatý, L.; Blaikie, R.; Schwefel, H.G.L.; Sedlmeir, F. Broadband second-harmonic generation in an x-cut lithium tetraborate whispering gallery mode resonator. *Opt. Lett.* **2025**, *50*, 5246–5249. [CrossRef]
27. Tian, F.; Wang, Y.; Huang, W.; Fang, X.; Guo, S.; Zhou, T. Ultra-Compact Topological Photonic Crystal Rainbow Nanolasers Operating in the 1550 nm Telecom Band with Wavelength-Scale Mode Volumes. *Adv. Mater.* **2025**, *37*, e05699. [CrossRef]
28. Biondi Vaccariello, A.M. Femtosecond laser machining of microchannels in hollow core fibres. *Nat. Rev. Phys.* **2025**, *7*, 236. [CrossRef]
29. Wang, Z.; Zhang, X.; Zhong, L.; Qiu, J. Femtosecond Laser Refractive Surgery: Reshaping the Cornea With Technical Advances. *Laser Photonics Rev.* **2025**, *19*, e01307. [CrossRef]
30. Duan, R.; Thung, Y.T.; Zhang, Z.; Durmusoglu, E.G.; He, Y.; Xiao, L.; Lee, C.X.X.; Lew, W.S.; Zhang, L.; Li, H.; et al. Colloidal Nanoplatelets-Based Soft Matter Technology for Photonic Interconnected Networks: Low-Threshold Lasing and Polygonal Self-Coupling Microlasers. *Laser Photonics Rev.* **2024**, *18*, 2300745. [CrossRef]
31. Duan, R.; Zhang, Q.; Thung, Y.T.; Zhou, X.; Yin, T.; Ao, Y.; Xiao, L.; Zhang, Z.; Lee, C.X.X.; Ren, T.; et al. Continuous-Wave Pumped Self-Assembled Colloidal Topological Lasers. *Adv. Mater.* **2025**, *37*, 2416635. [CrossRef] [PubMed]
32. Wang, Z.; Cui, Q.; Tan, Y.; Chen, F. WGM Photonic Molecules as a Platform for Stable Pulsed Laser Emission Generation. *ACS Photonics* **2025**, *12*, 5528–5536. [CrossRef]
33. Ceppe, J.B.; Féron, P.; Mortier, M.; Dumeige, Y. Dynamical Analysis of Modal Coupling in Rare-Earth Whispering-Gallery-Mode Microlasers. *Phys. Rev. Appl.* **2019**, *11*, 064028. [CrossRef]
34. Pathak, K.; Puri, S.; Pant, R. Microresonator Brillouin laser and multi-Stokes generation at 2 m. *Phys. Rev. Res.* **2024**, *6*, 023062. [CrossRef]
35. Sumetsky, M. Whispering-gallery-bottle microcavities: The three-dimensional etalon. *Opt. Lett.* **2004**, *29*, 8–10. [CrossRef]
36. Gorodetsky, M.L.; Fomin, A.E. Geometrical theory of whispering-gallery modes. *IEEE J. Sel. Top. Quantum Electron.* **2006**, *12*, 33–39. [CrossRef]
37. Sumetsky, M. Delay of Light in an Optical Bottle Resonator with Nanoscale Radius Variation: Dispersionless, Broadband, and Low Loss. *Phys. Rev. Lett.* **2013**, *111*, 163901. [CrossRef]
38. Benner, R.E.; Barber, P.W.; Owen, J.F.; Chang, R.K. Observation of Structure Resonances in the Fluorescence Spectra from Microspheres. *Phys. Rev. Lett.* **1980**, *44*, 475–478. [CrossRef]
39. Hill, S.C.; Benner, R.E. Morphology-dependent resonances associated with stimulated processes in microspheres. *J. Opt. Soc. Am. B* **1986**, *3*, 1509–1514. [CrossRef]
40. Lam, C.; Leung, P.T.; Young, K. Explicit asymptotic formulas for the positions, widths, and strengths of resonances in Mie scattering. *J. Opt. Soc. Am. B* **1992**, *9*, 1585–1592. [CrossRef]
41. Yang, S.; Wang, Y.; Sun, H. Advances and prospects for whispering gallery mode microcavities. *Adv. Opt. Mater.* **2015**, *3*, 1136–1162. [CrossRef]

42. Li, A.; Yu, J.; Zhang, M.; Lu, X.; Zhang, J.; Lewis, E.; Farrell, G.; Wang, P. An Yb^{3+}-Ho^{3+}Codoped Glass Microsphere Laser in the 2.0 μm Wavelength Regions. *IEEE Photonics Technol. Lett.* **2018**, *30*, 1543–1546. [CrossRef]
43. Zhu, S.; Shi, L.; Xiao, B.; Zhang, X.; Fan, X. All-Optical Tunable Microlaser Based on an Ultrahigh-Q Erbium-Doped Hybrid Microbottle Cavity. *ACS Photonics* **2018**, *5*, 3794–3800. [CrossRef]
44. Zhu, S.; Xiao, B.; Jiang, B.; Shi, L.; Zhang, X. Tunable Brillouin and Raman microlasers using hybrid microbottle resonators. *Nanophotonics* **2019**, *8*, 931–940. [CrossRef]
45. Hao, X.; Zhao, S.; Gao, J.; Suo, L. All-optical tunable whispering gallery mode lasing in a PMMA-coated microcavity embedded with a high-efficiency nanoheater. *Opt. Laser Technol.* **2023**, *164*, 109527. [CrossRef]
46. Hao, X.; Zhao, H.; Zhao, S. All-optical tunable single-mode lasing in polymer-coated microresonators. *Opt. Laser Technol.* **2025**, *192*, 113773. [CrossRef]
47. Huang, W.; Huang, Y.; Li, B.; Wang, L.; Xu, J. All-optical tuning of cascaded Raman lasing in silica microsphere. *Appl. Phys. Lett.* **2025**, *127*, e05699. [CrossRef]
48. Ji, M.; Liu, K.; Chen, W.; Yi, X.; Wang, M.; Tian, L.; Meng, J. Fabrication of a high-power pump and signal combiner with an asymmetric tapered fiber bundle utilizing un-pretreated pump fibers. *Opt. Express* **2025**, *33*, 12349–12360. [CrossRef]
49. Mu, Z.; Yang, Z.; Han, X.; Li, Y.; Sun, X. Tapered No-Core fiber sensor coated with graphene oxide for the detection of human hemoglobin. *Opt. Fiber Technol.* **2025**, *94*,104351. [CrossRef]
50. Lei, F.; Murphy, R.M.J.; Ward, J.M.; Yang, Y.; Chormaic, S.N. Bandpass transmission spectra of a whispering-gallery microcavity coupled to an ultrathin fiber. *Photonics Res.* **2017**, *5*, 362–366. [CrossRef]
51. Wu, J.; Yang, D.; Chen, J.; Huang, X.; Chen, W.; Qiu, J.; Yang, Z.; Dong, G. Tapered fiber coupling of nanoparticle-coated silica microspheres for multi-wavelength upconversion whispering gallery mode lasers. *Photonics Res.* **2025**, *13*, 2668–2678. [CrossRef]
52. Wang, Y.; Li, H.; Zhao, L.; Liu, Y.; Liu, S.; Yang, J. Tapered optical fiber waveguide coupling to whispering gallery modes of liquid crystal microdroplet for thermal sensing application. *Opt. Express* **2017**, *25*, 918–926. [CrossRef] [PubMed]
53. Spillane, S.M.; Kippenberg, T.J.; Painter, O.J.; Vahala, K.J. Ideality in a Fiber-Taper-Coupled Microresonator System for Application to Cavity Quantum Electrodynamics. *Phys. Rev. Lett.* **2003**, *91*, 043902. [CrossRef] [PubMed]
54. Gao, J.; Wang, X.; Chen, Y.; Chen, T.; Qi, Y.; Yang, H.; Zheng, X. Multiple Fano resonances by MIM waveguide coupling whispering gallery mode resonator and application in Refractive index sensing. *Phys. Scr.* **2024**, *99*, 055554. [CrossRef]
55. Gorshkov, O.N.; Grishin, I.A.; Kasatkin, A.P.; Smetanin, S.V.; Churbanov, M.F.; Shushunov, A.N. Optical planar waveguides based on tungsten-tellurite glass fabricated by rf-sputtering. *J. Non-Cryst. Solids* **2018**, *480*, 70–73. [CrossRef]
56. Konopsky, V.N.; Alieva, E.V. Imaging biosensor based on planar optical waveguide. *Opt. Laser Technol.* **2019**, *115*, 171–175. [CrossRef]
57. Li, Y.; Lan, T.; Yang, D.; Wang, Z. Fabrication of ridge optical waveguide in thin film lithium niobate by proton exchange and wet etching. *Opt. Mater.* **2021**, *120*, 111433. [CrossRef]
58. Xu, C.F.; Yu, Y.; Lv, Q.; Yan, C.C.; Wang, X.D.; Liao, L.S. Rational self-assembly of polygonal organic microcrystals for shape-dependent multi-directional 2D optical waveguides. *Chin. Chem. Lett.* **2022**, *33*, 3255–3258. [CrossRef]
59. Soltani, M.; Ilchenko, V.; Matsko, A.; Savchenkov, A.; Schlafer, J.; Ryan, C.; Maleki, L. Ultrahigh Q whispering gallery mode electro-optic resonators on a silicon photonic chip. *Opt. Lett.* **2016**, *41*, 4375–4378. [CrossRef]
60. Chao, C.Y.; Guo, L.J. Biochemical sensors based on polymer microrings with sharp asymmetrical resonance. *Appl. Phys. Lett.* **2003**, *83*, 1527–1529. [CrossRef]
61. Santamaria-Botello, G.A.; Garcia Munoz, L.E.; Sedlmeir, F.; Preu, S.; Segovia-Vargas, D.; Atia Abdalmalak, K.; Llorente Romano, S.; Garcia Lamperez, A.; Malzer, S.; Doehler, G.H.; et al. Maximization of the optical intra-cavity power of whispering-gallery mode resonators via coupling prism. *Opt. Express* **2016**, *24*, 26503–26514.
62. Gorodetsky, M.L.; Ilchenko, V.S. Optical microsphere resonators: Optimal coupling to high-Q whispering-gallery modes. *J. Opt. Soc. Am. B* **1999**, *16*, 147–154.
63. Rowland, D.R.; Love, J.D. Evanescent wave coupling of whispering gallery modes of a dielectric cylinder. *IEE Proc. J. (Optoelectron.)* **1993**, *140*, 177–188.
64. Huang, S.H.; Dirmeier, T.; Shafiee, G.; Laiho, K.; Strekalov, D.V.; Leuchs, G.; Marquardt, C. Polarization-entangled photons from a whispering gallery resonator. *npj Quantum Inf.* **2024**, *10*, 85.
65. Shu, F.J.; Zou, C.L.; Sun, F.W. Perpendicular coupler for whispering-gallery resonators. *Opt. Lett.* **2012**, *37*, 3123–3125.
66. Bai, X.; Wang, D. Whispering-gallery-mode excitation in a microsphere by use of an etched cavity on a multimode fiber end. *Opt. Lett.* **2018**, *43*, 5512–5515.
67. Shu, F.; Jiang, X.; Zhao, G.; Yang, L. A scatterer-assisted whispering-gallery-mode microprobe. *Nanophotonics* **2018**, *7*, 1455–1460.
68. Liu, S.; Gu, Z.; Zhang, N.; Wang, K.; Xiao, S.; Lyu, Q.; Song, Q. End-fire injection of guided light into optical microcavity. *Appl. Phys. B* **2015**, *120*, 255–260.
69. Liu, S.; Sun, W.; Wang, Y.; Yu, X.; Xu, K.; Huang, Y.; Xiao, S.; Song, Q. End-fire injection of light into high-Q silicon microdisks. *Optica* **2018**, *5*, 612–616.

70. Wan, S.; Shu, F.J.; Niu, R.; Guo, G.C.; Zou, C.L.; Dong, C.H. Perpendicular coupler for standing wave excitation and wavelength selection in high-Q silicon microresonators. *Opt. Express* **2020**, *28*, 15835–15843.
71. Zambrana-Puyalto, X.; D'Ambrosio, D.; Gagliardi, G. Excitation Mechanisms of Whispering Gallery Modes with Direct Light Scattering. *Laser Photonics Rev.* **2021**, *15*, 2000528.
72. Ward, J.M.; Lei, F.; Vincent, S.; Gupta, P.; Mondal, S.K.; Fick, J.; Chormaic, S.N. Excitation of whispering gallery modes with a "point-and-play," fiber-based, optical nano-antenna. *Opt. Lett.* **2019**, *44*, 3386–3389.
73. Li, A.; Tian, K.; Yu, J.; Minz, R.A.; Ward, J.M.; Mondal, S.; Wang, P.; Nic Chormaic, S. Packaged whispering gallery resonator device based on an optical nanoantenna coupler. *Opt. Express* **2021**, *29*, 16879–16886.
74. Fu, W.Y.; Choi, H.W. Electrically injected InGaN microdisk lasers: A review of progress, challenges, and future prospects. *Prog. Quantum Electron.* **2024**, *95*, 100516. [CrossRef].
75. Xu, K.; Wan, P.; Liu, M.; Shi, D.; Kan, C.; Jiang, M. An electrically-pumped WGM microlaser realized in an n-AlGaN/n-ZnO:Ga microwire/Pt/MgO/p-GaN double-heterojunction device. *J. Mater. Chem. C* **2024**, *12*, 17818–17828. [CrossRef].
76. Ohtani, K.; Meng, B.; Franckié, M.; Bosco, L.; Ndebeka-Bandou, C.; Beck, M.; Faist, J. An electrically pumped phonon-polariton laser. *Sci. Adv.* **2019**, *5*, eaau1632. [CrossRef].
77. Choi, J.H.; Hayenga, W.E.; Liu, Y.G.; Parto, M.; Bahari, B.; Christodoulides, D.N.; Khajavikhan, M. Room temperature electrically pumped topological insulator lasers. *Nat. Commun.* **2021**, *12*, 3434.
78. Hayenga, W.E.; Garcia-Gracia, H.; Sanchez Cristobal, E.; Parto, M.; Hodaei, H.; LiKamWa, P.; Christodoulides, D.N.; Khajavikhan, M. Electrically Pumped Microring Parity-Time-Symmetric Lasers. *Proc. IEEE* **2020**, *108*, 827–836. [CrossRef].
79. Toropov, N.; Cabello, G.; Serrano, M.P.; Gutha, R.R.; Rafti, M.; Vollmer, F. Review of biosensing with whispering-gallery mode lasers. *Light Sci. Appl.* **2021**, *10*, 42.
80. Van Nguyen, T.; Van Pham, N.; Mai, H.H.; Duong, D.C.; Le, H.H.; Sapienza, R.; Ta, V.D. Protein-based microsphere biolasers fabricated by dehydration. *Soft Matter* **2019**, *15*, 9721–9726.
81. Duan, R.; Hao, X.; Li, Y.; Li, H. Detection of acetylcholinesterase and its inhibitors by liquid crystal biosensor based on whispering gallery mode. *Sens. Actuators B Chem.* **2020**, *308*, 127672.
82. Duan, R.; Li, Y.; He, Y.; Yuan, Y.; Li, H. Quantitative and sensitive detection of lipase using a liquid crystal microfiber biosensor based on the whispering-gallery mode. *Analyst* **2020**, *145*, 7595–7602.
83. Mai, H.H.; Nguyen, T.T.; Giang, K.M.; Do, X.T.; Nguyen, T.T.; Hoang, H.C.; Ta, V.D. Chicken albumen-based whispering gallery mode microlasers. *Soft Matter* **2020**, *16*, 9069–9073.
84. Guo, Z.; Qin, Y.; Chen, P.; Hu, J.; Zhou, Y.; Zhao, X.; Liu, Z.; Fei, Y.; Jiang, X.; Wu, X. Hyperboloid-Drum Microdisk Laser Biosensors for Ultrasensitive Detection of Human IgG. *Small* **2020**, *16*, 2000239.
85. Schubert, M.; Woolfson, L.; Barnard, I.R.M.; Dorward, A.M.; Casement, B.; Morton, A.; Robertson, G.B.; Appleton, P.L.; Miles, G.B.; Tucker, C.S.; et al. Monitoring contractility in cardiac tissue with cellular resolution using biointegrated microlasers. *Nat. Photonics* **2020**, *14*, 452–458.
86. Titze, V.M.; Caixeiro, S.; Di Falco, A.; Schubert, M.; Gather, M.C. Red-Shifted Excitation and Two-Photon Pumping of Biointegrated GaInP/AlGaInP Quantum Well Microlasers. *ACS Photonics* **2022**, *9*, 952–960.
87. Titze, V.M.; Caixeiro, S.; Dinh, V.S.; König, M.; Rübsam, M.; Pathak, N.; Schumacher, A.L.; Germer, M.; Kukat, C.; Niessen, C.M.; et al. Hyperspectral confocal imaging for high-throughput readout and analysis of bio-integrated microlasers. *Nat. Protoc.* **2024**, *19*, 928.
88. Wang, J.; Song, Y.; Dou, X.; Sun, J.; Yang, X.; Zhang, Y.; Liu, Z.; Li, Y.; Li, H. Liquid Crystal Microcavity Biosensors for Real-Time Liver Injury Monitoring via Whispering Gallery Mode Laser. *Research* **2025**, *8*, 0824.
89. Zhang, Z.; Wang, Z.; Xu, Z.; Gao, Q.; Liu, P.; Ren, J.; Li, M.; Zhou, C.; Liao, Q.; Fu, H. Soft Lithography to Fabricate 3D Patterning Organic Microrings towards High-Performance Near-Infrared Laser Arrays. *Adv. Opt. Mater.* **2018**, *6*, 1800219.
90. Wang, Z.; Xu, Z.; Cui, J.; Tan, J. Power output correction model of narrow linewidth ring fiber laser filtered with whispering gallery mode resonator. *Chin. Opt. Lett.* **2024**, *22*, 031401.
91. Du, Y.; Zou, C.L.; Zhang, C.; Wang, K.; Qiao, C.; Yao, J.; Zhao, Y.S. Tuneable red, green, and blue single-mode lasing in heterogeneously coupled organic spherical microcavities. *Light Sci. Appl.* **2020**, *9*, 151.
92. Jiang, B.; Zhu, S.; Wang, W.; Li, J.; Dong, C.H.; Shi, L.; Zhang, X. Room-temperature Continuous-Wave Upconversion White Microlaser Using a Rare-earth-Doped Microcavity. *ACS Photonics* **2022**, *9*, 2956–2962.
93. Ge, K.; Shi, X.; Xu, Z.; Libin, C.; Guo, D.; Li, S.; Zhai, T. Full-color WGM lasing in nested microcavities. *Nanoscale* **2021**, *13*, 10792–10797.
94. Chen, W.; Wang, L.; Liu, R.; Shen, H.; Du, J.; Fan, F. Self-Assembled and Wavelength-Tunable Quantum Dot Whispering-Gallery-Mode Lasers for Backlight Displays. *Nano Lett.* **2023**, *23*, 437.
95. Ren, G.; Yang, L.; Yao, C.; Wang, X.; Pu, L.; Li, K.; Zhang, L.; Li, P. Mid-Infrared Ultraflat Broadband Supercontinuum Generation with 10 dB Bandwidth of 2340 nm in a Tapered Fluorotellurite Fiber. *Photonics* **2025**, *12*, 297.

96. Gong, W.; Hu, J.; Wang, Z.; Wei, Y.; Li, Y.; Zhang, T.; Zhang, Q.; Liu, T.; Ning, Y.; Zhang, W.; et al. Recent advances in laser gas sensors for applications to safety monitoring in intelligent coal mines. *Front. Phys.* **2022**, *10*, 1058475.
97. Wang, X.; Cong, H.; Xie, C.; Li, Y.; Xu, G.; Wang, Y.; Xu, C.; Xue, C. Preparation and loss analysis of Ge on Si SWIR optical strip waveguides. *Appl. Phys. Lett.* **2024**, *125*, 093502.
98. Behzadi, B.; Hossein-Zadeh, M. On the Performance of Intracavity Gas Sensors Based on Whispering-Gallery Microlasers. *IEEE Sens. J.* **2020**, *20*, 9772–9778.
99. Wu, L.; He, P.; Xu, H.; Li, B.; Yantang, H. Methane Sensor Based on High-Q Microsphere Whispering Gallery Mode. *J. Phys. Conf. Ser.* **2023**, *2597*, 012018.
100. Wang, H.; Weng, L.; Yu, W. All-optical Tuning of Microsphere Whispering Gallery Mode Resonance Wavelength to Lock to the DFB Laser Wavelength for Using in CH4 Detection. *J. Phys. Conf. Ser.* **2023**, *2464*, 012014.
101. Sumaria, V.; Tadigadapa, S. Whispering-Gallery-Mode Optical Microshell Resonator Infrared Detector. *IEEE Sens. J.* **2021**, *21*, 2634–2641.
102. D'Ambrosio, D.; Capezzuto, M.; Aiello, R.; Delli Santi, M.G.; Sorgi, A.; Malara, P.; Avino, S.; Giorgini, A.; Maddaloni, P.; Consolino, L.; et al. Infrared-to-THz Detection and Spectroscopy with Whispering-Gallery-Mode Microresonators. *Adv. Photonics Res.* **2022**, *3*, 2200147.
103. Richardson, D.J.; Fini, J.M.; Nelson, L.E. Space-division multiplexing in optical fibres. *Nat. Photonics* **2013**, *7*, 354–362.
104. Poddubrovskii, N.R.; Drobyshev, R.V.; Lobach, I.A.; Kablukov, S.I. Fiber Lasers Based on Dynamic Population Gratings in Rare-Earth-Doped Optical Fibers. *Photonics* **2022**, *9*, 613.
105. Li, H.; Wang, Z.; Wang, L.; Tan, Y.; Chen, F. Selective 1.3 μm Laser Emission via Coupled Microlaser for Laser Resonance Tuning. *ACS Photonics* **2024**, *11*, 1508–1516.
106. Rabie, G.O. Structural, Spectroscopic, and Optical Properties of Na_2O–SiO_2 Glass Network Doped with Er_2O_3. *Silicon* **2025**, *17*, 1859–1871.
107. Tripathi, R.; Fanai, A.L.; Mishra, H. Influence of Yb^{3+} ion concentration on energy transfer mechanism, thermal quenching and up-conversion luminescence in zinc tellurite glasses doped with Tm^{3+} ions. *J. Mol. Struct.* **2025**, *1349*, 143801.
108. Wang, Z.; Cui, Q.; Zhao, J.; Tan, Y.; Chen, F. Low-threshold single-mode laser operation from a 35-pm-diameter Er:YAG microdisk laser. *Opt. Lett.* **2025**, *50*, 4858–4861.
109. Van Hoi, P.; Ha, C.; Hung, H. Long-band emission of microsphere lasers based on erbium-doped sol-gel silica-alumina glasses. *Appl. Phys. Lett.* **2005**, *87*, 161110.
110. Yang, Y.; Lei, F.; Kasumie, S.; Xu, L.; Ward, J.M.; Yang, L.; Chormaic, S.N. Tunable erbium-doped microbubble laser fabricated by sol-gel coating. *Opt. Express* **2017**, *25*, 1308–1313.
111. Li, A.; Li, W.; Zhang, M.; Zhang, Y.; Wang, S.; Yang, A.; Yang, Z.; Lewis, E.; Brambilla, G.; Wang, P. Tm^{3+}-Ho^{3+} codoped to lurite glass microsphere aser in the 1.47 μm wavelength region. *Opt. Lett.* **2019**, *44*, 511–513.
112. Loiko, P.; Kifle, E.; Brasse, G.; Thouroude, R.; Starecki, F.; Benayad, A.; Braud, A.; Laroche, M.; Girard, S.; Gilles, H.; et al. In-band pumped Tm,Ho:LiYF4 waveguide laser. *Opt. Express* **2022**, *30*, 11840–11847.
113. Fang, Z.; Chormaic, S.N.; Wang, S.; Wang, X.; Yu, J.; Jiang, Y.; Qiu, J.; Wang, P. Bismuth-doped glass microsphere lasers. *Photonics Res.* **2017**, *5*, 740–744.
114. Wan, Y.; Norman, J.; Li, Q.; Kennedy, M.J.; Liang, D.; Zhang, C.; Huang, D.; Zhang, Z.; Liu, A.Y.; Torres, A.; et al. 1.3 μm submilliamp threshold quantum dot micro-lasers on Si. *Optica* **2017**, *4*, 940–944.
115. Lei, L.; Dong, Q.; Gundogdu, K.; So, F. Metal Halide Perovskites for Laser Applications. *Adv. Funct. Mater.* **2021**, *31*, 2010144. [CrossRef].
116. Soto-Montero, T.; Morales-Masis, M. Laser Deposition of Metal Halide Perovskites. *ACS Energy Lett.* **2024**, *9*, 4199–4208. [CrossRef].
117. Li, H.; Wang, Z.; Wang, L.; Tan, Y.; Chen, F. 27% slope efficiency in a WGM microcavity enabled by an Yb:YAG crystalline film. *Opt. Lett.* **2023**, *48*, 5359–5362. [CrossRef].
118. Li, X.; Wang, D.N. A Whispering-Gallery Mode Microsphere Resonator Based on Optical Fiber with an Open Microcavity. *J. Light. Technol.* **2021**, *39*, 3466–3470.
119. Chang, T.C.; Hong, K.B.; Lai, Y.Y.; Chou, Y.H.; Wang, S.C.; Lu, T.C. ZnO-Based Microcavities Sculpted by Focus Ion Beam Milling. *Nanoscale Res. Lett.* **2016**, *11*, 319.
120. Tang, B.; Dong, H.; Sun, L.; Zheng, W.; Wang, Q.; Sun, F.; Jiang, X.; Pan, A.; Zhang, L. Single-Mode Lasers Based on Cesium Lead Halide Perovskite Submicron Spheres. *ACS Nano* **2017**, *11*, 10681–10688.
121. Frigenti, G.; Berneschi, S.; Farnesi, D.; Pelli, S.; Righini, G.C.; Soria, S.; Dumeige, Y.; Féron, P.; Ristić, D.; Prudenzano, F.; et al. Rare earth-doped glass whispering gallery mode micro-lasers. *Eur. Phys. J. Plus* **2023**, *138*, 679.
122. Lu, X.; Zhang, Y.; Ren, J.; Lewis, E.; Farrell, G.; Yang, A.; Yang, Z.; Wang, P. Chalcogenide glasses with embedded ZnS nanocrystals: Potential mid-infrared laser host for divalent transition metal ions. *J. Am. Ceram. Soc.* **2018**, *101*, 666–673.

123. Lu, X.; Li, J.; Yang, L.; Ren, J.; Sun, M.; Yang, A.; Yang, Z.; Jain, R.K.; Wang, P. Broadband mid-infrared (2.5–5.5 μm) emission from Co2+/Fe2+ codoped chalcogenide glass ceramics. *Opt. Lett.* **2020**, *45*, 2676–2679.
124. Anelli, F.; Venck, S.; Cozic, S.; Prudenzano, F. S-Tapered Fluoride Optical Fiber for Refractive Index Sensing in the Mid-Infrared. *J. Light. Technol.* **2025**, *43*, 5982–5988.
125. Zhao, X.; Yao, N.; Zhang, X.; Zhang, L.; Tao, G.; Li, Z.; Liu, Q.; Zhao, X.; Xu, Y. Optimizing Evanescent Efficiency of Chalcogenide Tapered Fiber. *Materials* **2022**, *15*, 3834.
126. Miura, K.; Tanaka, K.; Hirao, K. Laser oscillation of a Nd^{3+}-doped fluoride glass microsphere. *J. Mater. Sci. Lett.* **1996**, *15*, 1854–1857.
127. Caï, Z.P.; Xu, H.Y.; Stéphan, G.M.; Feron, P.; Mortier, M. Red-shift in Er: ZBLALiP whispering gallery mode laser. *Opt. Commun.* **2004**, *229*, 311–315.
128. Lissillour, F.; Feron, P.; Dubreuil, N.; Dupriez, P.; Stephan, G.M.; Poulain, M. Whispering-gallery mode Er-ZBLAN microlasers at 1.56 μm. In *Proceedings of the Laser Resonators II, San Jose, CA, USA, 27–29 January 1999*; SPIE: Bellingham, WA, USA, 1999; Volume 3611, pp. 199–205.
129. Yang, K.; Dai, S.; Wu, Y.; Nie, Q. Fabrication and characterization of Ge-Ga-Sb-S glass microsphere lasers operating at ∼1.9 μm. *Chin. Phys. B* **2018**, *27*, 117701.
130. Deng, Y.; Jain, R.K.; Hossein-Zadeh, M. Demonstration of a cw room temperature mid-IR microlaser. *Opt. Lett.* **2014**, *39*, 4458–4461.
131. Tebeneva, T.S.; Shitikov, A.E.; Benderov, O.V.; Lobanov, V.E.; Bilenko, I.A.; Rodin, A.V. Ultrahigh-Q WGM microspheres from ZBLAN for the mid-IR band. *Opt. Lett.* **2022**, *47*, 6325–6328.
132. Razova, A.A.; Fadeev, M.A.; Rumyantsev, V.V.; Utochkin, V.V.; Dubinov, A.A.; Aleshkin, V.Y.; Mikhailov, N.N.; Dvoretsky, S.A.; Gusev, N.S.; Shengurov, D.V.; et al. Whispering gallery mode HgCdTe laser operating near 4 μm under Peltier cooling. *Appl. Phys. Lett.* **2023**, *123*, 161105.
133. Meisenheimer, S.K.; Fürst, J.U.; Buse, K.; Breunig, I. Continuous-wave optical parametric oscillation tunable up to an 8 μm wavelength. *Optica* **2017**, *4*, 189–192.
134. Aktas, O.; Peacock, A.C. Laser Thermal Processing of Group IV Semiconductors for Integrated Photonic Systems. *Adv. Photonics Res.* **2021**, *2*, 2000159. [CrossRef].
135. Kim, Y.; Assali, S.; Ge, J.; Koelling, S.; Luo, M.; Luo, L.; Joo, H.J.; Tan, J.; Shi, X.; Ikonic, Z.; et al. Mid-infrared group IV nanowire laser. *Sci. Adv.* **2025**, *11*, eadt6723. [CrossRef].
136. Liu, T.; Seidel, L.; Concepción, O.; Reboud, V.; Chelnokov, A.; Capellini, G.; Oehme, M.; Grützmacher, D.; Buca, D. Electrically Pumped GeSn Micro-Ring Lasers. *IEEE J. Sel. Top. Quantum Electron.* **2025**, *31*, 8100307. [CrossRef].
137. Kryzhanovskaya, N.V.; Moiseev, E.I.; Polubavkina, Y.S.; Maximov, M.V.; Kulagina, M.M.; Troshkov, S.I.; Zadiranov, Y.M.; Lipovskii, A.A.; Baidus, N.V.; Dubinov, A.A.; et al. Electrically pumped InGaAs/GaAs quantum well microdisk lasers directly grown on Si(100) with Ge/GaAs buffer. *Opt. Express* **2017**, *25*, 16754–16760. [CrossRef].
138. Wu, X.; Tian, Z.; Cong, H.; Wang, Y.; Edy, R.; Huang, G.; Di, Z.; Xue, C.; Mei, Y. Infrared tubular microcavity based on rolled-up GeSn/Ge nanomembranes. *Nanotechnology* **2018**, *29*, 42LT02. [CrossRef].
139. Spillane, S.; Kippenberg, T.; Vahala, K. Ultralow-threshold Raman laser using a spherical dielectric microcavity. *Nature* **2002**, *415*, 621–623.
140. Lin, G.; Diallo, S.; Saleh, K.; Martinenghi, R.; Beugnot, J.C.; Sylvestre, T.; Chembo, Y.K. Cascaded Brillouin lasing in monolithic barium fluoride whispering gallery mode resonators. *Appl. Phys. Lett.* **2014**, *105*, 231103.
141. Guo, C.; Che, K.; Cai, Z.; Liu, S.; Gu, G.; Chu, C.; Zhang, P.; Fu, H.; Luo, Z.; Xu, H. Ultralow-threshold cascaded Brillouin microlaser for tunable microwave generation. *Opt. Lett.* **2015**, *40*, 4971–4974.
142. Lu, J.; Xu, C.; Nan, H.; Zhu, Q.; Qin, F.; Manohari, A.G.; Wei, M.; Zhu, Z.; Shi, Z.; Ni, Z. SERS-active ZnO/Ag hybrid WGM microcavity for ultrasensitive dopamine detection. *Appl. Phys. Lett.* **2016**, *109*, 073701.
143. Andrianov, A.; Anashkina, E. Single-mode silica microsphere Raman laser tunable in the U-band and beyond. *Results Phys.* **2020**, *17*, 103084.
144. Mao, W.; Li, Y.; Jiang, X.; Liu, Z.; Yang, L. A whispering-gallery scanning microprobe for Raman spectroscopy and imaging. *Light Sci. Appl.* **2023**, *12*, 247.
145. Haehnle, B.; Lamla, M.; Sparrer, K.M.; Gather, M.C.; Kuehne, A.J. Narrow stimulated resonance Raman scattering and WGM lasing in small conjugated polymer particles for live cell tagging and tracking. *Adv. Opt. Mater.* **2021**, *9*, 2001553.
146. Jiang, X.F.; Xiao, Y.F.; Yang, Q.F.; Shao, L.; Clements, W.R.; Gong, Q. Free-space coupled, ultralow-threshold Raman lasing from a silica microcavity. *Appl. Phys. Lett.* **2013**, *103*, 101102.
147. Tian, J.; Lin, G. Magnesium Fluoride Brillouin and Raman Microlaser. *J. Light. Technol.* **2024**, *42*, 2118–2123.
148. Savchenkov, A.A.; Matsko, A.B.; Ilchenko, V.S.; Solomatine, I.; Seidel, D.; Maleki, L. Tunable optical frequency comb with a crystalline whispering gallery mode resonator. *Phys. Rev. Lett.* **2008**, *101*, 093902.
149. Savchenkov, A.; Matsko, A.; Liang, W.; Ilchenko, V.; Seidel, D.; Maleki, L. Kerr combs with selectable central frequency. *Nat. Photonics* **2011**, *5*, 293–296.

150. Rueda, A.; Sedlmeir, F.; Kumari, M.; Leuchs, G.; Schwefel, H.G. Resonant electro-optic frequency comb. *Nature* **2019**, *568*, 378–381.
151. Chen, B.; Zhou, Y.; Liu, Y.; Ye, C.; Cao, Q.; Huang, P.; Kim, C.; Zheng, Y.; Oxenløwe, L.K.; Yvind, K.; et al. Integrated optical vortex microcomb. *Nat. Photonics* **2024**, *18*, 625–631. [CrossRef]
152. Wang, Y.; Zheng, J.; Li, Y.; Gu, Y.; Sun, B.; Zhang, Z. Broadband continuous Kerr-Raman comb generation via transverse mode interaction in microcavities. *J. Light. Technol.* **2025**, *43*, 7714–7719. [CrossRef]
153. Song, Y.; Hu, Y.; Lončar, M.; Yang, K. Hybrid Kerr-electro-optic frequency combs on thin-film lithium niobate. *Light Sci. Appl.* **2025**, *14*, 270. [CrossRef]
154. Sun, Z.; Liu, S.; Liu, Z.; Qin, W.; Chen, D.; Xu, G.; Wu, C. FRET acceptor suppressed single-particle photobleaching in semiconductor polymer dots. *Opt. Lett.* **2016**, *41*, 2370–2373. [CrossRef]
155. Zhou, J.; Huang, T.; Fang, Z.; Wu, R.; Zhou, Y.; Liu, J.; Zhang, H.; Wang, Z.; Wang, M.; Cheng, Y. Laser diode-pumped compact hybrid lithium niobate microring laser. *Opt. Lett.* **2022**, *47*, 5599–5601. [CrossRef]
156. Tang, M.; Park, J.S.; Wang, Z.; Chen, S.; Jurczak, P.; Seeds, A.; Liu, H. Integration of III-V lasers on Si for Si photonics. *Prog. Quantum Electron.* **2019**, *66*, 1–18. [CrossRef]
157. Yi, R.; Zhang, X.; Yuan, X.; Wang, J.; Zhang, Q.; Zhang, Y.; Fang, L.; Zhang, F.; Fu, L.; Tan, H.H.; et al. Integrating a Semiconductor Nanowire Laser in a Silicon Nitride Waveguide. *ACS Photonics* **2024**, *11*, 2471–2479. [CrossRef]

Disclaimer/Publisher's Note: The statements, opinions and data contained in all publications are solely those of the individual author(s) and contributor(s) and not of MDPI and/or the editor(s). MDPI and/or the editor(s) disclaim responsibility for any injury to people or property resulting from any ideas, methods, instructions or products referred to in the content.